Phase diagrams for multicomponent systems containing corium and products of its interaction with NPP materials (CORPHAD) Phase 2

PROGRESS REPORT

01/07/03 – 30/06/04

INVESTIGATION OF BINARY OXIDIC SYSTEMS: SYSTEM ZrO_2-FeO

Project title	Phase diagrams for multicomponent systems containing corium and products of its interaction with NPP materials (CORPHAD, #1950.2)	
Customer	ISTC	
File specification	CORPHAD/RCP-0402	
Place of project implementation	FGUP Alexandrov Research Institute of Technology (NITI) of the Russian Federal Agency for Atomic Energy Russia 188540, Sosnovy Bor of Leningrad Oblast, NITI	
Project manager	Name Signature	Yu. N. Aniskievich
	Date	October, 2004

Authors

Professor	V.B. Khabensky
Doctor	S.V. Bechta
Doctor	V.S. Granovsky
Academician	V.V. Gusarov
	S.A. Vitol
	E.V. Krushinov
Professor	Yu.B. Petrov
Doctor	S.Ju. Kotova
Doctor	A. A. Sulatskey
Doctor	I.V. Kulagin
Doctor	D.B. Lopukh
Doctor	A.Yu. Pechenkov
Doctor	L.P. Mezentseva
Doctor	A.V. Merzlyakov
	V.G. Blizniuk
	V.R. Bulighin
	E.M. Beliaeva
	E.K. Kaliago
	N.E. Kamensky
	A.V. Lisenko
	A.P. Martinov
	V.V. Martinov
	E.V. Shevchenko
	A.A. Chertkov
	V.I. Almjashev
	S.K. Kuchaeva
	N.A. Lomanova
	V.F. Popova

CONTENTS

Summary

The report offers descriptions of and main findings from the tests in the framework of the ISTC #1950/2 CORPHAD Project, which have been performed to investigatie the ZrO_2-FeO binary oxidic system in an inert atmosphere. The tests were performed using such classical methods, as DTA (DSC), specimens' annealing at different temperatures followed by physico-chemical analyses, etc., and original methods, like visual polythermal analysis in the cold crucible and in the Galakhov microfurnace.

Liquidus temperatures for a broad range of compositions were determined, solubility limits of wustite in zirconia with due regard to polymorphism of the latter found, the eutectic point position refined, and a phase diagram for the ZrO_2-FeO system constructed.

Introduction

The diagram **ZrO_2 – FeO** is of interest for describing phase equilibriums in molten corium. This binary diagram is basic for a more general ternary system **Zr – Fe – O** which will also be investigated within the framework of the CORPHAD Project.

Phase equilibriums in the **ZrO_2 – FeO** system have been studied by Fischer and Hoffman [1]. This work yielded the eutectic point which corresponds to 3 mass % ZrO_2 at a temperature of 1330±15°C, and a domain of ZrO_2-based solid solutions (SS) within 4 mass % FeO at 1450°C. The findings from this study are given in Fig. 1. The studied temperature range is obviously limited, and the domain of ZrO_2-based SS is defined vaguely. Fig. 1 also shows the liquidus line calculated using the MULTICOMDIA program created at ISC, and the calculated eutectic point which corresponds to 15 mass % ZrO_2. The calculated eutectic composition differs greatly from the composition obtained in the work [1].

It should be noted that it is a technically difficult task to create conditions for the existence of stoichiometric FeO in a melt. No information on the melt stoichiometry in the performed tests is given in the work [1].

The above-mentioned circumstances stipulated objectives of the present research, namely:

- refining the eutectic position on the phase diagram;
- determining liquidus temperatures;
- defining more exactly the components' solubility limits in the solid state.

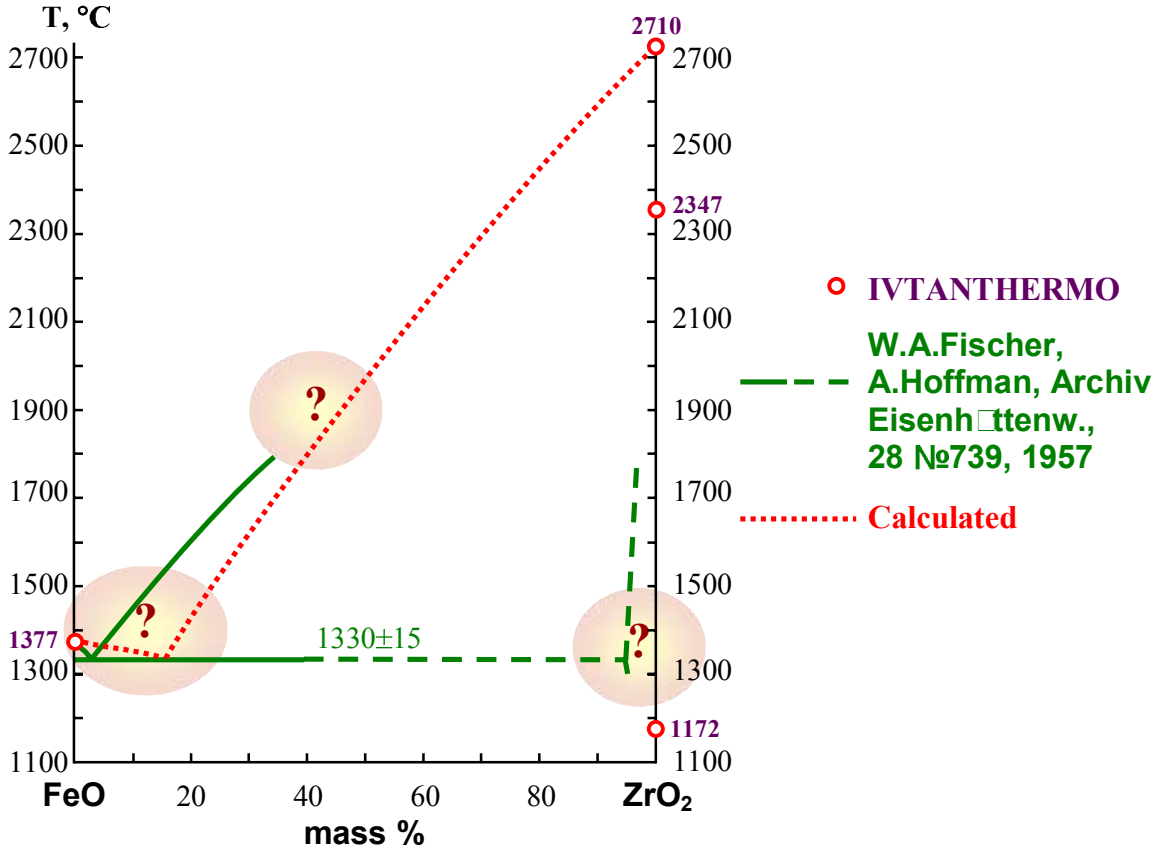

Fig. 1. ZrO_2 – FeO phase diagram: solid and dotted lines are based on the data from the work [1]; fine-dotted line is based on the calculations performed by the authors

1. Methodologies and experimental facilities

At present there is no universally accepted method of phase diagram studies, which would provide reliable and accurate data on phase transformation temperatures, including solidus and liquidus temperatures, in the systems having a fixed composition and wide variations of atmosphere. Therefore, the continuous improvement of methods for the phase diagram studies was combined with the application of complementary methodologies, which increased the reliability of resulting data.

1.1. Visual polythermal analysis in a cold crucible

One of the classical methods of thermal analysis is the visual polythermal analysis (VPA) [3]. Its procedure includes the slow cooling of a crucible with melt in the furnace until first crystals appear on the molten pool surface. At this stage the surface temperature is registered; due to the slow cooling rate (1-2°C/min) and in absence of subcooling it is close to liquidus temperature. In accordance with [3] the error of this method does not exceed 10°C.

In most cases the application of this and other classical methods for the studies of corium-based systems is limited due to the high chemical activity of the melt. It interacts with crucible materials, which results in the melt pollution and, very often, in the failure to take measurements because of the crucible destruction. For this reason we have put forward a new VPA method applicable for the conditions of induction melting in a cold crucible (VPA IMCC), which lately has undergone a substantial adjustment for corium studies. Practically, it is the only method, which can be applied for studying high-temperature melts containing iron oxides.

The main IMCC peculiarity influencing the analysis accuracy and the character of melt crystallization is the thermal inhomogeneity of the pool contained within the water-cooled walls of the cold crucible. During the melt cooling its crystallization takes place both on the pool surface (like during VPA in the refractory or hot crucible) and on the interface of melt – bottom/side crusts produced on the cold crucible walls. This may result in the depletion of the refractory component in the melt; and the phase diagram point corresponding to the initial melt composition is located in the primary crystallization field of the refractory component. By the time, when first crystals appear on the molten pool surface its composition may not correspond to the initial melt composition. In the IMCC case the melt composition at the stage of crystal appearance is determined from the sample taken from the melt surface and subjected to the posttest physico-chemical analysis.

The originally-developed version of the VPA IMCC included the following stages:

1. The superheated molten pool was produced from the charge having a specified composition. The thickness of bottom crust was measured.
2. Power deposition in the melt was slowly decreased by stepping down the inductor voltage. The appearance of first crystals on the pool surface was registered. The first crystals on the melt surface were included into a viscous film having a darker coloring as compared to the initial melt.
3. The melt sample was taken as soon as the film appeared.
4. Frame-by-frame video-sequence was examined after the test, and the minimum temperature of the melt co-existing with film was determined.
5. Posttest physico-chemical analysis of the melt sample and identification of its composition were made.

This methodology has been checked using well-known phase diagrams, in particular ZrO_2-Nb_2O_5. Along with that, the measurements comparing the VPA IMCC data with DTA and DSC (differential scanning calorimetry) have been repeatedly performed. The resulting experimental data enabled to evaluate the liquidus temperature measurement error. It is the same

as the pyrometer error in the composition range close to the eutectic. For refractory compositions with high fusion range the error is 50-75 °C. The above-described method was used in the studies carried out within the CIT and ENTHALPY projects [2, 5 - 8]. The molten pool surface behavior was recorded on video (Fig. 1.1), and video-recorder was combined with pyrometer (3), which added the 50 Hz- frequency temperature measurements and position of the sighting spot to each still of the video sequence (Fig. 1.2) carried out using camera (3) and video recorder (6) (Fig. 1.1). Temperature on the molten pool surface was measured by the spectral ratio pyrometer RAYTEK MR1-SC. The camera monitored the region limited by the pyrometer shaft diameter, i.e. 22 mm. The pyrometer sighting spot is about 6 mm. The internal diameter of the cold crucible is 38 mm. The region not included into the recording is an 8-mm wide ring along the crucible wall.

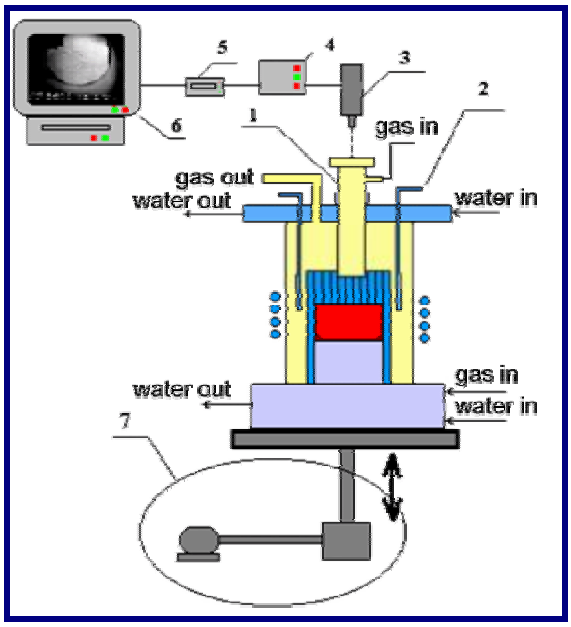

1-pyrometer shaft, 2- movable water-cooled electromagnetic screen, 3- pyrometer combined with video camera, 4- MDAS, 5- device for inserting measurement results into video-frames, 6- monitor/video recorder, 7- drive for vertical crucible movement

Fig. 1.1. Combined pyrometry – video recording system

It should be noted that the posttest analysis of melt composition, for which liquidus temperature was measured, complicates the methodology and delays the availability of results. In order to exclude changes in the melt composition at the VPA IMCC and, respectively, to reduce the complexity of posttest analysis, the method was improved by creating conditions for local cooling of the melt surface, the bulk of which was superheated. It was achieved (Fig. 1.1) by using the water-cooled electromagnetic screen, which was moved along the vertical crucible axis. When positioned against the thin surface layer of the superheated pool it provided the local temperature reduction and did not cause melt composition changes.

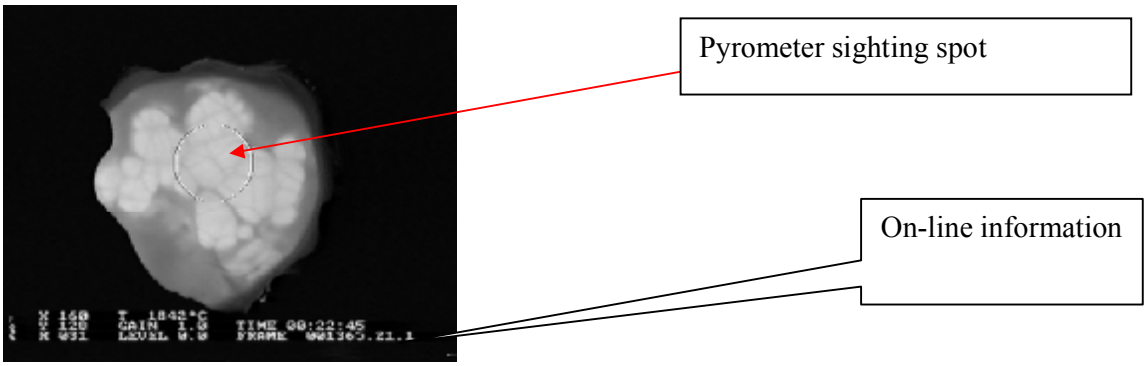

The melt surface temperature measured in the pyrometer sighting spot (white circle) and the time of the experiment are given in bottom lines

Fig. 1.2. A still of the molten pool surface

Fig. 1.3. gives an example of an experimental thermogram combined with the image of molten pool surface.

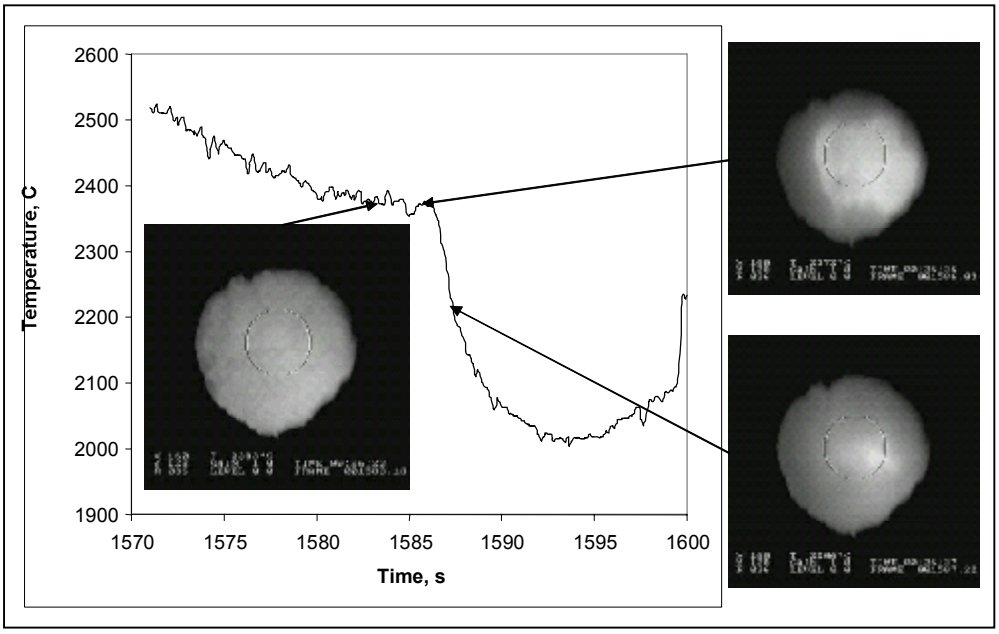

Fig. 1.3. A thermogram combined with images of the melt surface

At present the refined VPA IMCC methodology includes the following stages:

1. The superheated molten pool is produced from the charge having a specified composition. The thickness of bottom crust is measured.
2. A melt sample is taken.
3. The surface of superheated molten pool undergoes local cooling performed by moving the electromagnetic screen; the temperature and pool surface behavior are recorded.
4. The video is analyzed in a frame-by-frame way, the minimum melt temperature is determined.
5. Chemical posttest analysis of the melt sample and identification of its composition are performed (if necessary).

Let us consider the main sources of errors typical of the VPA IMCC methodology:

- Error in temperature and melt composition measurements. The relative error of pyrometric measurements integrating the error of a corresponding channel in the modular data acquisition system (MDAS) is 1%. Section 2.4 explains the error in determining composition by different methods of posttest analysis.

- Error caused by the melt subcooling. It has been confirmed by publications that in the non-equilibrium conditions the melt crystallization starts only after its subcooling to a certain degree. The degree of subcooling ΔT is a melt composition-specific, and in accordance with [10] it does not exceed 20-50 K. The direct measurement of ΔT of high-temperature oxidic melts under the IMCC conditions is not possible. The ΔT of melts can be derived from crystallization experiments using other methods. E.g., the direct ΔT measurements were conducted during the examination of the temperature axial gradient and subcooling on the crystallization front, when sapphire crystals were produced by the Stepanov method [9]. I was demonstrated that during the drawing of aluminium oxide crystals through the draw plate at a linear speed of 3-5 mm/min, subcooling ΔT of the melt on the meniscus was 30-45 °C.

- Error caused by the temperature gradient and free convection of the molten pool in the IMCC conditions, which can be as high as 50 °C [10].

Testing of the described methodology in the experiments with melts having well-known phase diagrams (Table 1.1), and the comparison of the VPA IMCC data with the results of DTA an DSC, in which the high-temperature microscope and Galakhov microfurnace were used, have shown that the total VPA IMCC error in determining liquidus temperature is equal to the temperature measurements error of the eutectics region compositions (or of pure oxides). In case of compositions having a wide fusibility range (over 200°C), and in their high-temperature region in particular, the error can be sufficiently higher, but, as a rule, it does not exceed 50-75 °C.

Table 1.1. Comparison of melting temperatures (1), eutectics temperatures (2,3) and liquidus temperatures (4,5) determined by VPA IMCC and published data

#	Composition, mass %	VPA IMCC data, °C	Published data, °C	Source
1	100% Al_2O_3	2053	(2047-2054)±7	Samsonov, 1978
2	12% ZrO_2 88% Nb_2O_3	1411	1430	Toropov et al., 1969
3	19% ZrO_2 81% Fe_3O_4	1515	1520	Fischer and Hoffmann, 1957
4	21% ZrO_2 79% FeO	1611	1620	Fischer and Hoffmann, 1957
5	36.3% ZrO_2 73.7% FeO	1825	1835	Fischer and Hoffmann, 1957

A special methodology was used for determining the eutectics composition. According to it the melt was crystallized in the close-to-equilibrium conditions, which were achieved by slow (5-10 mm/h) uninterrupted driving of crucible versus inductor using drive (7) (Fig. 1.1). The posttest physicochemical analysis of samples from the last-to-crystallize ingot region enables to determine the eutectics composition with the 1-2 mass% error. The eutectics temperature (equal to solidus in case of simple eutectics systems) is determined by the VPA IMCC during the melting of corium having eutectics composition and later checked by other methods of thermal analysis.

The posttest analysis of ingots, produced by the equilibrium crystallization method described above, also enables a qualitative determination of the miscibility gap presence/absence in the system using the data on the ingot microstructure [11].

1.2. Galakhov method

Liquidus temperature has also been determined by the visual polythermal analysis in the Galakhov microfurnace [12].

Fig. 1.4 presents the microfurnace schematics. The microfurnace consists of a water-cooled metallic bottom, it is equipped by pipes for the evacuation of air and inert gas supply. The electrode holders are inserted into the furnace through the bottom. They are screened from it by mica plates, and the sealing liquid insulates them from the environment.

The spiral-shaped tungsten heater is incorporated into the electrode holders. The furnace experimental section is a 20-22 mm-high and 5.5-6 mm-wide cylinder (the zone of isothermal heating inside the heater). To reduce heat dissipation and achieve close-to-isothermal conditions the heater is surrounded by a molybdenum screen fastened to one of the supports.

A special device is used for putting a specimen into the microfurnace. The tested specimen is designed to have about 2 mm in diameter. It is inserted into the "eye" of a molybdenum or iridium 0.1-0.3 mm-thick wire-holder. The specimen location in the center of the isothermal zone is ensured by the specified wire length.

The microfinance is also designed for the specimen quenching (from the isothermal zone it can be dropped into the water-cooled channel).

The microfurnace is insulated from the environment by the water-cooled bell-jar. When heating is conducted in the inert atmosphere (to build up positive pressure) a special ring is used to press the jar to the base. The jar top has a quartz viewing window. The specimen melting and other transformations are recorded by the video system.

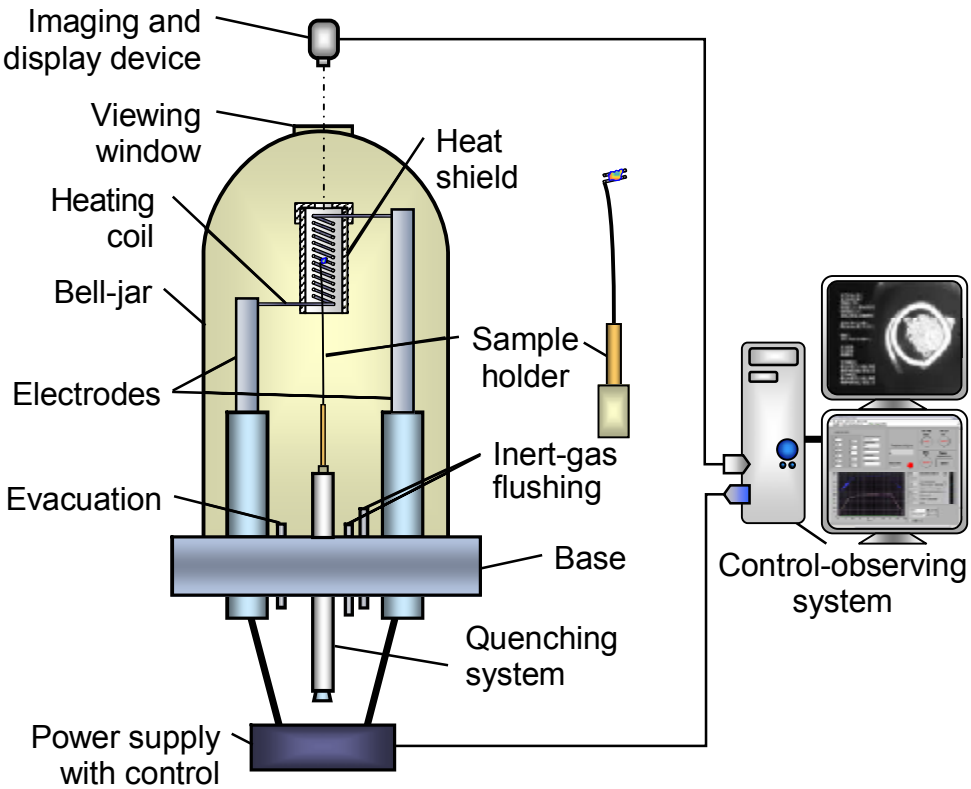

Fig. 1.4. Schematics of the Galakhov microfurnace

If the vacuum is not deep enough, the tungsten heater can get oxidized and tungsten oxide can be transferred to the specimen and cover it as a film, which may result in the melting

temperature measurement errors. To avoid this the microfurnace is evacuated to $>10^{-5} – 10^{-6}$ atm. using a fore-evacuation and diffusion pumps. Following this the furnace is sparged with inert gas at least twice.

The temperatures, at which the observable changes in the specimen conditions take place, are determined from the curve of isothermal zone temperature vs. power supplied to the heater. In order to construct the curve a series of reference meltings is performed, in which the substances having the established melting temperatures are used (Pt; Pd; Ag; Au; Cu; Al_2O_3 and others).

The heating is controlled automatically, and the heating and cooling curve is predetermined. The video recording is provided with temperature values recalculated from the power in the heater. The video signal is further processed on the computer. When the specimen spreads over the molybdenum (iridium) holder, the liquidus temperature is assumed to be reached.

There are at least four arguments for taking the specimen spreading in the Galakhov microfurnace for the liquidus temperature:

- heating produces a liquid phase very quickly (within 10 seconds). From this it can be inferred that we are fixing the point of low viscosity, because the high spreading rate is the indicator of such conditions;
- the specimen is prepared in such a way that its refractory phase would form a skeleton structure (rod quenching of a specimen under the IMCC conditions). In this way the prepared specimen starts spreading only after the skeleton destruction. It happens only in the case when the solid phase volume in the system does not exceed 5%.
- the specimen fast quenching is performed by its dropping from the heating zone. The microstructure of quenched specimens features the absence of unmolten regions, which testifies to the complete fusion of specimens;
- data of the visual polythermal analysis in the Galakhov microfurnace are confirmed by the data of differential thermal analysis, which is considered to be a classical method for phase diagram construction; and also by the data of other methods, the VPA IMCC in particular.

The range of experimental temperature measurements in the microfurnace is 900-2300°C. The experiments were conducted in the $10^{-5} – 10^{-6}$ atm. vacuum or in the inert atmosphere (argon, helium). The microfurnace is designed for experiments, when the inert gas pressure can be up to 1 atm. The maximum error of measurements in the mentioned temperature range is ±25°C.

1.3. Differential thermal analysis

Determination of T_{sol} and, when possible, of T_{liq} was made by DTA using the HTA analyzer of Ukrainian make (DTA, up to 2100°C, in vacuum or inert gas) and NETZSCH STA 429 (DSC/TG; up to 1600°C, in vacuum and specified atmosphere).

The DTA was used only for determining solidus temperature, because liquidus measurements were not technically feasible due to the interaction between the resulting melt and crucible, which caused the sample composition changes. The specimens for studies were prepared from quenched melt samples or ingots. Solidus temperature was determined from the start of endothermic effect at specimen heating.

2. IMCC tests of the CORD series

2.1. Initial charge materials analysis

When preparing the test, iron oxide (II) was checked for the main substance and impurities content The content of metallic iron Fe^0 was determined by the copper sulphate method.

The method is based on the copper replacement with metallic iron at treating a batch of corium powder with the copper sulphate solution [13]. Fe^{2+} ions, equivalent to Fe_{met}, are titrated off with the potassium dichromate solution in the presence of sodium diphenylaminesulphonate, a redox indicator.

The method allows determination of metallic iron in powdered corium samples with the iron content of less than 0.5%.

The reactions are described by the following equations:

$$Fe+CuSO_4=FeSO_4+Cu\downarrow$$

$$6FeSO_4+K_2Cr_2O_7+7H_2SO_4=Cr_2(SO_4)_3+3Fe_2(SO_4)_3+K_2SO_4+7H_2O$$

Metallic iron content (C, mass %) is calculated by formula:

$$C_{Fe\ met.}= (100\times(a-b)\times T)/B,$$

where:
- a is the quantity of 0.1B potassium dichromate solution used for titration, ml;
- b is the quantity of 0.1B potassium dichromate solution used for the solution titration in the control test, ml;
- T is the titre of 0.1B potassium dichromate solution expressed in grammes of metallic iron;
- B is the batch that corresponds to the aliquot part of solution taken for titration, g.

The content of Fe(II) and Fe(III) was determined by photocolorimetry with orthophenanthroline. The method is meant for the determination of iron oxides content in samples of the uranium-bearing corium without uranium separation [14]. The range of identified iron concentrations is 0.5-2.0 mg/dm^3. The total relative error of the method does not exceed ±3%, provided the measured optical densities are within 0.2-0.6 range.

The method is based on the reaction of orthophenanthroline (1.10-phenanthroline) with ferrous iron ions, which yields a complex compound with an orange-red colouring. The colour intensity is proportionate to the concentration of iron. Since the bond strength of the complex compound is high (formation constant is $9.8\cdot10^{21}$), optical density does not depend on pH in the 2-9 range. Colouring develops rapidly at pH=3.0-3.5 in presence of excessive orthophenanthroline and keeps stable within several weeks. In more acid solutions the colouring develops slower and is less intense. The direct iron determination is possible at its mass concentration from 0.5 to 2.0 mg/dm^3 [15]. The method allows separate determination of ferrous iron and total iron in a solution. The amount of ferric iron is calculated from the difference between the content of iron (II) and total iron [16]. The iron mass concentration (X) in mg/dm^3 is calculated by formula:

$$X=(C\times25)/V ,$$

where:
C is the iron concentration found from the calibrating diagram, mg/dm^3;
V is the volume of the analyzed aliquot iron sample, cm^3;
25 is the volume to which the sample has been diluted, cm^3.

The composition of charge components is given in Tab 2.1.

Table 2.1. Charge components composition

Components	Main substance content, %	Impurities, mass %	Notes
ZrO_2 powder, dispersivity <100 μm	(ZrO_2+HfO_2) > 99.3	Al_2O_3<0.03; Fe_2O_3<0.05; CaO<0.03; MgO<0.02; SiO_2<0.2; TiO_2<0.1; P_2O_5<0.15; (Na_2O+K_2O)<0.02.	Passport data
FeO*	68.4	Fe_2O_3-29.6; Fe-0.5	Chemical analysis results
FeO**	68.2	Fe_2O_3-30.0; Fe-0.7	Chemical analysis results
FeO***	66.3	Fe_2O_3-32.4; Fe-0.9	Chemical analysis results
Fe	>99.9	Si-0.0005; Mg-0.0001; Cu-0.0001; Ni-0.019; Pb-0.0001; Zn-0.00028	Passport data

*- used in CORD 1-5,9
**- used in CORD 10-13, 15, 16
***- used in CORD 24

2.2. Test specifications

Altogether, 14 tests have been performed. Their specifications are given in Tab 2.2.

Table 2.2. Specifications of CORD tests

CORD	Crucible charge composition, mass %				Charge mass, g	Test objective
	ZrO_2	FeO	Fe	Fe, getter		
1 & 2	2.97	87.23	8.81	0.99	161.59	Eutectic determination
3 & 4	49.50	44.97	4.54	0.99	131.30	T_{liq} measurement
5	69.31	26.98	2.73	0.99	131.30	
9	16.15	75.73	7.41	0.70	142.18	Ingot drawing, eutectic determination
10	49.75	45.77	4.48	-	145.73	T_{liq} measurements
11	34.55	59.04	5.78	0.63	146.87	
12	34.77	59.41	5.82	-	145.95	
13	24.81	68.48	6.71	-	146.11	
15	59.76	36.65	3.59	-	140.56	
16	79.84	18.36	1.80	-	140.28	
24	64.16	31.62	3.23	0.99	298.90	T_{liq} measurements, ingot drawing
29A	94.10	4.90	1.00	-	136.00	$T_{cub \rightarrow tetr}$

All tests were performed in an inert atmosphere of argon. In order to obtain FeO, metallic (carbonyl) iron was introduced into the furnace, and for the FeO stoichiometry a getter (also carbonyl iron) was additionally introduced into the melt. The getter was not used in the tests 10,

12-16 in order to avoid the influence of metallic iron in the samples on T_{liq} measurements in the Galakhov microfurnace. The tests were carried out at the Rasplav 2 and Rasplav 3 test facilities with crucibles 25 and 40 mm across, respectively.

2.3. Experimental procedures

Practically all experimental procedures for T_{liq} determination were identical and included:

- Charge materials preparation and their thorough mixing in argon.
- Loading of the specified composition into the furnace and its purging with argon.
- Molten pool production and its superheating above T_{liq}.
- Molten pool depth and bottom crust measurement.
- Melt sampling.
- Decrease of power in the melt, until the appearance of films/crusts (CORD 1-5) (the initially developed version of the VPA IMCC technique).
- Screen shifting (downward), screen position fixing at the appearance of films/crusts (CORD 9-16, 24).
- Repeated shifts of the screen to the fixed position and video recording of films/crusts formation for determining T_{liq}.
- Heating termination. Pool surface video recording.
- Ingot extraction from the crucible for the subsequent analysis.

The furnace depressurization occurred in CORD 1 and 3 and the tests were aborted. At the pool depth measuring in CORD 11, a part of the tungsten probe broke off and fell into the melt. Due to tungsten dissolution and formation of a film at the melt surface, the VPA IMCC could not be done and the test was terminated. In CORD 4,5 crystallization of the total molten pool volume was additionally carried out by means of introducing a water-cooled crystallizer into the pool (Fig. 2.1). The crystallizer represented a cylinder with a diameter 5 mm smaller than the crucible internal diameter.

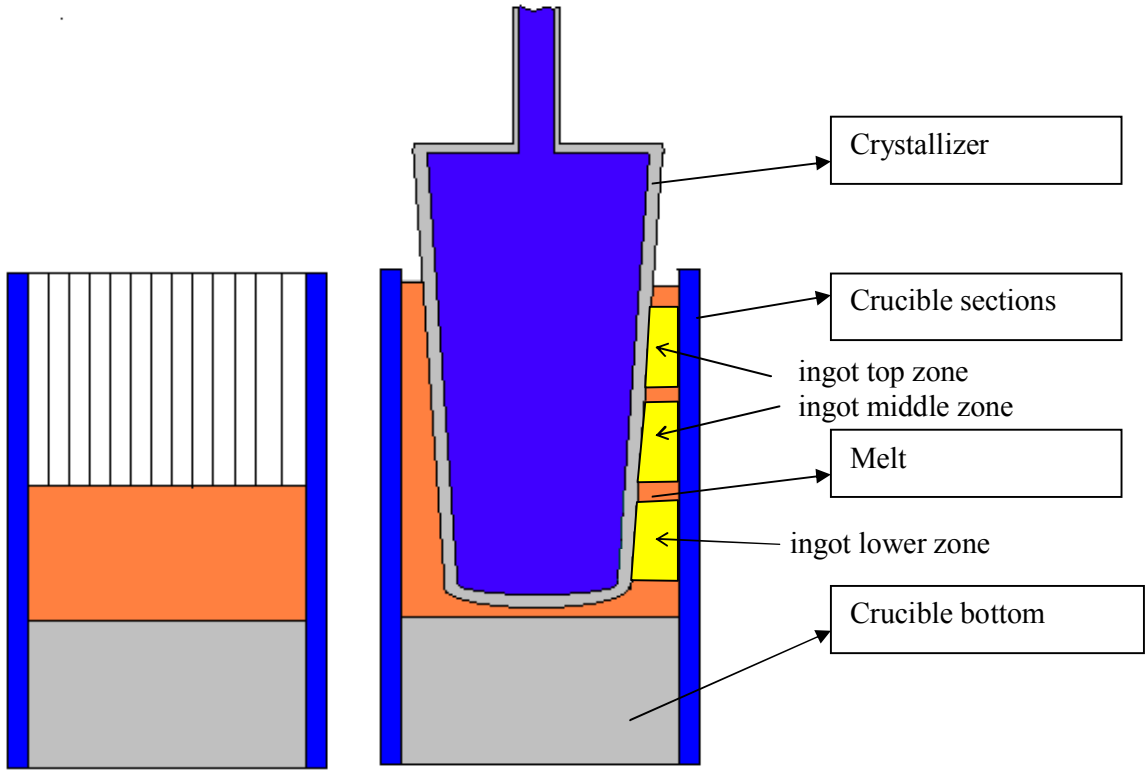

Fig. 2.1. Diagram of melt quenching in cold crucible

The procedures for determining the eutectic composition and temperature were different from the described above and included:

- Charge materials preparation and their thorough mixing in argon.
- Loading of the specified composition into the furnace and its purging with argon.
- Molten pool production and its superheating above T_{liq}.
- Molten pool depth and bottom crust measurement.
- Crucible mechanical shifting downward relative to the inductor, until the generator responded to the shifting by the anode current decrease.
- Crucible movement mechanism switching on (Item 7, Fig.1.1).
- Ingot drawing from the inductor zone at 5-10 mm/h for approximately 7-8 hours.
- Heating termination. Pool surface video recording.
- Ingot extraction from the crucible.
- Ingot longitudinal cutting and preparation of a template for SEM/EDX.
- Identification of the last liquid phase (eutectic) crystallization area from the SEM/EDX results, and cutting a sample from the area.

The total of two tests – CORD 2 and 9 – were devoted to determining the eutectic composition. In CORD 2 the crucible movement mechanism was absent, and slow crystallization and eutectic extrusion were achieved by smoothly decreasing power in the melt. CORD 9 employed the updated version of said technique in order to confirm correctness of the CORD 2 results. The test 29A was aimed at producing an ingot of a high-temperature SS.

2.4. Posttest analysis

In the course of the tests, prior to measuring T_{liq} (of the eutectic) by means of VPA IMCC, the melt was sampled (quenched on the rod, or taken into special samplers) for determining its coordinates (melt composition) within the phase diagram and for verifying quality of the initial oxides stoichiometry.

After completing the tests, the produced corium ingots were cut along the longitudinal axis to prepare templates for SEM/EDX and specimens to be analyzed in the Galakhov microfurnace. Melt samples were also used for preparing specimens ('scales') for the Galakhov microfurnace analysis.

2.4.1. Chemical analysis

All the works on samples preparation for the analysis were performed in argon. At first, the melt samples and the ingot were completely crushed down to grains sized no more than 2 mm. Then an average sample was taken by quartering and milled into particles sized no more than 50 μm.

Both the ingot and samples were checked for the content of Fe^0, Fe^{2+}, Fe^{3+}.

The content of metallic iron Fe^0 was determined by the copper sulphate method and that of Fe(II) and Fe(III) – by photocolorimetry with orthophenanthroline.

The results of Fe^0, Fe^{2+} and Fe^{3+} determination are presented in Tab. 2.1.

Table 2.3. Chemical analysis results for samples from CORD 10, 12, 13, 15, 16 and 24 tests

CORD	Initial charge composition, mass %		Sample	Content, mass %		
	ZrO_2	FeO		Fe^0	Fe^{2+}	Fe^{3+}
10	50	50	corium ingot average sample	1.0	33.9	2.8
			melt #1 sample	0.4	36.3	4.0
12	35	65	corium ingot average sample	1.7	42.1	3.5
			melt #1 sample	1.3	48.1	3.0
13	25	75	corium ingot average sample	5.3	46.6	4.2
			melt #2 sample	1.5	51.4	6.3
15	60	40	corium ingot average sample	0.4	25.7	2.2
			melt #1 sample	0.3	26.6	4.8
16	80	20	corium ingot average sample	2.3	12.7	0.3
24	65	35	melt #2 sample	0.2	29.2	4.5

It should be noted that the presence of Fe^0, Fe^{3+} in the samples indicates to the decomposition of wustite into alpha iron and magnetite during crystallization. To our opinion, this circumstance has no effect on the measured T_{liq}, but may influence the ultimate solubility of iron oxides in zirconia.

The data from Tab. 2.3 were used for calculating the total content of FeO_y in the samples and the value of 'y' by the way of transferring Fe^{2+} and Fe^{3+} into stable oxides FeO and Fe_2O_3. The content of ZrO_2 in the samples was calculated as 100% minus FeO_y.

Table 2.4 shows the results of chemical analysis of samples from CORD 10, 12, 13, 15, 16 and 24 (in terms of oxides).

Table 2.4. Chemical analysis results for samples from CORD 10, 12, 13, 15, 16 and 24 (in terms of oxides)

CORD	Initial charge composition, mass %/mass %		Sample	Content, mass %		y
	ZrO_2	FeO		ZrO_2	FeO_y	
10	50	50	corium ingot average sample	50.8	49.2	1.06
			melt #1 sample	46.5	53.5	1.09
12	35	65	corium ingot average sample	38.4	61.6	1.05
			melt #1 sample	31.8	68.2	1.05
13	25	75	corium ingot average sample	28.0	72.0	0.99
			melt #2 sample	22.6	77.4	1.07
15	60	40	corium ingot average sample	63.0	37.0	1.07
			melt #1 sample	58.2	41.8	1.11
16	80	20	corium ingot average sample	80.9	19.1	0.90
24	65	35	melt #2 sample	55.4	44.6	1.11

The last column in the Table contains values of the oxygen index in FeOy, and it may be seen from the data that the composition of iron oxides is close to wustite ($FeO_{1.053}$) practically in all the tests. The Table does not include the analysis results for the samples from CORD 4 and 5, as excess iron (getter) in the melt makes the existence of iron oxides in the form of wustite inevitable.

As can be seen from figures in the Table, the melt samples are richer in the fusible component (FeO_y) than the specified charge and the corium ingot average composition owing to the refractory component (ZrO_2) crystallization in the crust on the cold surfaces bounding the pool.

Tab. 2.5 shows errors of the performed chemical analyses.

Table 2.5. Chemical analyses errors

Element	Error, relative %	Determination method
Fe^0	10	Copper sulphate
Fe^{+2}	5	Photocolorimetry
Fe^{+3}	5	

2.4.2. X-ray fluorescence (XRF) analysis

XRF was used for the samples' elemental analysis using the SPARK-1M spectrometer designed for the successive qualitative and quantitative determination of 66 chemical elements from Sc(21) to U(92) in a wide range of their concentrations in samples.

For this analysis, a special technique of compacted pellets was applied to the preparations. Two-layer pellets composed of a mixture of zirconium and iron oxides taken in different proportions were fused by the IMCC method in a small crucible to serve as calibration samples.

All the works on samples preparation for the analysis were performed in argon. At first, the samples were completely crushed down to grains sized no more than 2 mm. Then an average sample was taken by quartering and milled into particles sized no more than 50 μm.

Tables 2.6 contains the XRF results (in terms of oxides) for the samples from the tests.

Table 2.6. XRF results for corium samples from CORD 4, 5, 9, 10, 12, 13, 15 and 24 (in terms of oxides)

CORD	Sample	Content, mass %	
		ZrO_2	FeO_y
4	quenched molten corium top part	41.0	59.0
	quenched molten corium middle part	47.0	53.0
	quenched molten corium bottom part	51.0	49.0
5	quenched molten corium top part	66.4	33.6
	quenched molten corium middle part	66.0	34.0
	quenched molten corium bottom part	70.2	29.8
9	corium ingot average sample	16.7	83.3
10	melt #1 sample	44.2	55.8
12	melt #1 sample	29.6	70.4
13	melt #2 sample	20.9	79.1
15	melt #1 sample	58.9	41.1
24	melt #2 sample	53.4	46.6

The XRF results given in the table coincide with those of chemical analysis (Tab. 2.4) within the measurement error limits.

The analysis results for CORD 4 and 5 show that the composition of the crystallizer-quenched melt differs along the ingot height: the fusible component (FeO_y) content is higher in its upper part than in the lower one. Moreover, the larger the iron oxide content in the initial melt, the bigger is the difference. Obviously, the reason is the crystallization of a more refractory phase (ZrO_2) at the crystallizer end at its introduction into the melt and this phase depletion in the upper layers of the surrounding melt.

When constructing the phase diagram, melt concentrations (with T_{liq} measured by VPA IMCC) have been determined from the results of chemical analysis of melt samples taken before the VPA measurements.

2.4.3. Material balance data from the tests

In order to calculate material balances for the tests, initial components of the charge and fused products were weighed with 0.1 g accuracy.

Mass balance data from CORD 2, 4, 5, 9, 10-13, 15, 16 and 24 are given in Tab. 2.7

Table 2.7. Material balance data from CORD 2, 4, 5, 9, 10, 12, 13, 15, 16 and 24

Test	Introduced into melt, g		Collected, g	
CORD 2	ZrO_2	[4.8]	Ingot	148.6
	FeO	141.0	Sample (inside spoon)	0.5
	Fe	15.8	Sample (spoon top)	1.1
			Corium from probe	3.1
			Leakages	3.0
			Spillages	5.0
	Σ	**161.6**	**Σ**	**161.3**
	Debalance	**0.3**		
CORD 4	ZrO_2	65.0	Sample (spoon top)	1.5
	FeO	59.0	Sample (inside spoon)	1.1
	Fe	7.3	Corium from probe	4.2
			Ingot	116.4
			Spillages	8.0
	Σ	**131.3**	**Σ**	**131.2**
	Debalance	**0.1**		
CORD 5	ZrO_2	91.0	Sample (spoon top)	2.3
	FeO	35.4	Sample (inside spoon)	0.6
	Fe	4.9	Corium from probe	3.7
			Ingot	117.2
			Spillages	7.0
	Σ	**131.3**	**Σ**	**130.8**
	Debalance	**0.5**		
CORD 9	ZrO_2	23.0	Corium from probe	3.8
	FeO	107.7	Ingot	136.1
	Fe	11.6	Spillages	0.1
	Σ	**142.3**	**Σ**	**140.0**
	Debalance	**2.3**		
CORD 10	**ZrO_2**	72.5	**Ingot**	93.5
	FeO	66.7	**Sample**	2.7
	Fe	6.5	**From probe**	19.0
			Spillages	4.0
			Accretions on sections	26.3
	Σ	145.7	**Σ**	**145.5**
	Debalance	**0.2**		

CORD 12	**ZrO_2**	50.8	**Ingot**	111.6
	FeO	86.7	**Sample 1**	2.6
	Fe	8.5	**Sample 2**	7.3
			From probe	7.3
			Spillages	3.6
			Accretions on sections	8.3
			Leakages	3.5
	Σ	**146.0**	**Σ**	**144.2**
	Debalance		**1.8**	
CORD 13	**ZrO_2**	36.3	**Sample 1**	4.3
	FeO	100.1	**Sample 2**	1.8
	Fe	9.8	**From probe**	4.3
			Ingot	124.8
			Spillages	4.1
			Leakages	5.7
	Σ	**146.2**	**Σ**	**145.0**
	Debalance		**1.2**	
CORD 15	**ZrO_2**	84.0	**Ingot**	127.0
	FeO	51.5	**Sample**	4.7
	Fe	5.0	**From probe**	2.3
			Spillages	5.7
	Σ	**140.5**	**Σ**	**139.7**
	Debalance		**0.8**	
CORD 16	**ZrO_2**	112.0	**From probe**	5.2
	FeO	25.8	**Ingot**	102.6
	Fe	2.5	**Spillages**	16.2
			Accretions	14.6
	Σ	140.3	**Σ**	138.6
	Debalance		**1.7**	
CORD 24	**ZrO_2**	191.8	**Ingot**	252.8
	Fe	12.6	**Sample 1**	1.9
	FeO	94.5	**Sample 2**	3.1
			Spillages	25.6
			Rod sample 1	2.0
			Rod sample 2	5.5
			From probe	5.0
	Σ	**298.9**	**Σ**	**295.9**
	Debalance		**3.0**	

Small values of debalance in the tests indicate to representativity of the conducted research.

2.4.4. SEM/EDX analysis of ingots

Microstructure, elemental and phase composition of the ingots were studied by means of scanning electron microscopy (SEM) and energy dispersive X-ray spectrometry (EDX).

The study employed the CamScan MV2300 and ABT-55 scanning electron microscope, and the OxfordLink microprobe attachment was used for the elemental analysis of the samples' regions marked for examination.

The spectral characteristic was taken for each sample for determining its integral composition and that for each separate phase. The quantitative analysis was made by comparing spectral intensity of the reference (superpure, specially prepared substances) and studied samples. The used references U, Zr, Cr, Fe, Si, Ca, Ni were a part of the microprobe attachment set.

The threshold of reliable element identification depends on its sequential number in the Mendeleyev's periodic table and varies from 0.1 mass % for light elements to 0.3 mass % for heavy ones in the case with the Oxford Link Pentafet EDX analyzer, with which the CamScan MV2300 microscope is equipped, and is 0.5 mass % for the Link EDX analyzer of the ABT-55 microscope. The identification of smaller quantities of an element is unreliable.

The EDX analyzer of the ABT-55 microscope is insensitive to light elements (to oxygen, for instance), therefore the quantity of oxygen was determined with this instrument from the mass deficiency and the error was ~5 mass %.

When the Oxford Link Pentafet EDX analyzer is used for the oxygen content determination, the error does not exceed 0.3 mass %, as a rule, but the energy peaks overlapping happens when studying the iron-containing systems and it leads to an additional error in determining both oxygen and iron content.

The error of determining the bulk composition is the same as for separate phases determination. There are, however, a couple of notes to be made: firstly, the error of oxygen content determination increases significantly for the highly porous samples; secondly, the higher the degree of sample's heterogeneity is, the more the composition determined for a smaller region (depending on the sample type, the scanning field varies from 20x20 μm to 2x2 mm) will differ from the total samples' average composition determined, for instance, by XRF.

Analysis results for the ingot from CORD 2

The diagram of studying the ingot longitudinal section is given in Fig. 2.2. The results of the CORD 2 ingot analysis are presented in Figs. 2.3-2.4. The test was aimed at verifying the results of work [1], for instance, an alloy with eutectic composition was the target. This explains the choice of examination locations on the ingot template (Fig. 2.2). At the molten pool slow crystallization, the last (eutectic) melt would crystallize in the thermal centre of the ingot, somewhat closer to its upper part. In our case, this is zone 2.

Fig. 2.2. Template from CORD 2 with locations marked for examination

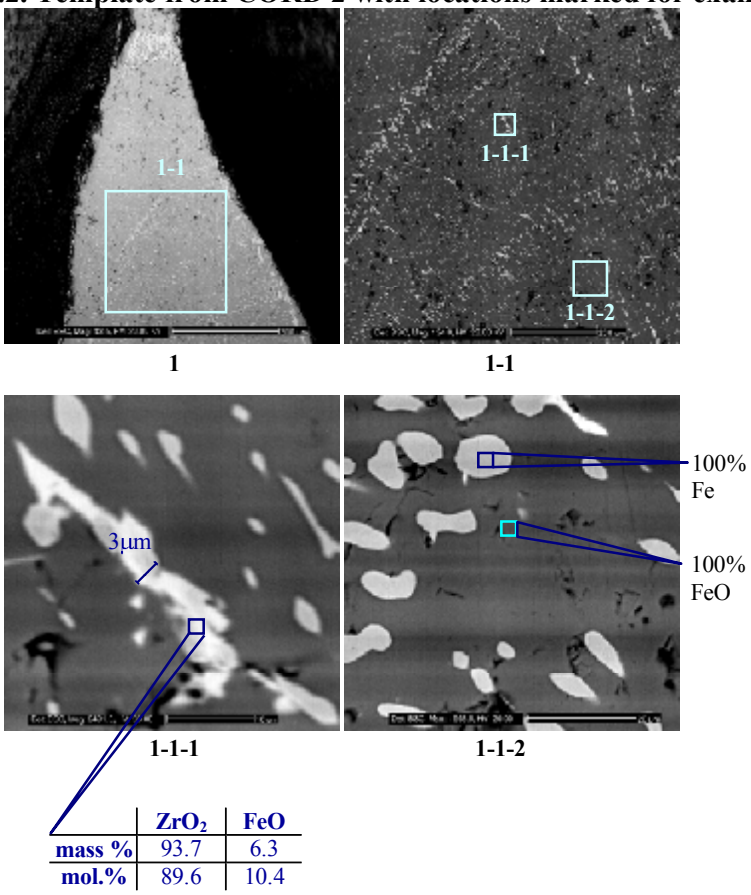

	ZrO_2	FeO
mass %	93.7	6.3
mol.%	89.6	10.4

Fig. 2.3. Micrographs of region 1 from the ingot and EDX results

The region 1-1 shows the microstructure of the ingot upper peripheral part which has formed through melt crystallization on crust layers while the pool level was decreasing as a result of shrinkage. The melt was slowly crystallized for 3 hours and therefore its level was slowly

lowering. Light-coloured layers of the crystallized excessive pure iron are clearly visible in the structure. The dominating phase is FeO, and this shows that the melt composition was in the domain of FeO primary crystallization.

The grains of FeO SS in ZrO_2 have seemingly formed in the subsolidus domain of the diagram at long exposure of this zone to a temperature below the eutectic point. Therefore, they should have a composition that would approximately correspond to the ultimate composition at the eutectic temperature. However, the content of 6.3 wt % FeO is seen as excessive and is not confirmed by further analyses. The FeO SS crystals in ZrO_2 are few, it being the consequence of a small amount of eutectic in this structure and the shift of its composition towards FeO.

The analyzed region 2 (Fig. 2.4) is more informative. The monophase layer arc of grey colour is the layer of FeO primary crystallization which also outlines the spherical area of the final liquid. This liquid microstructure (area 2-1-1, Fig. 2.4) indicates to the eutectic character of crystallization. The integral composition of the last eutectic liquid was found to be FeO / ZrO_2 = 83.6 / 16.4 mass %.

The analyzed grains of the FeO SS in ZrO_2 from this eutectic area were found to have the FeO / ZrO_2 composition ratio = 1.3 / 98.7 mass %.

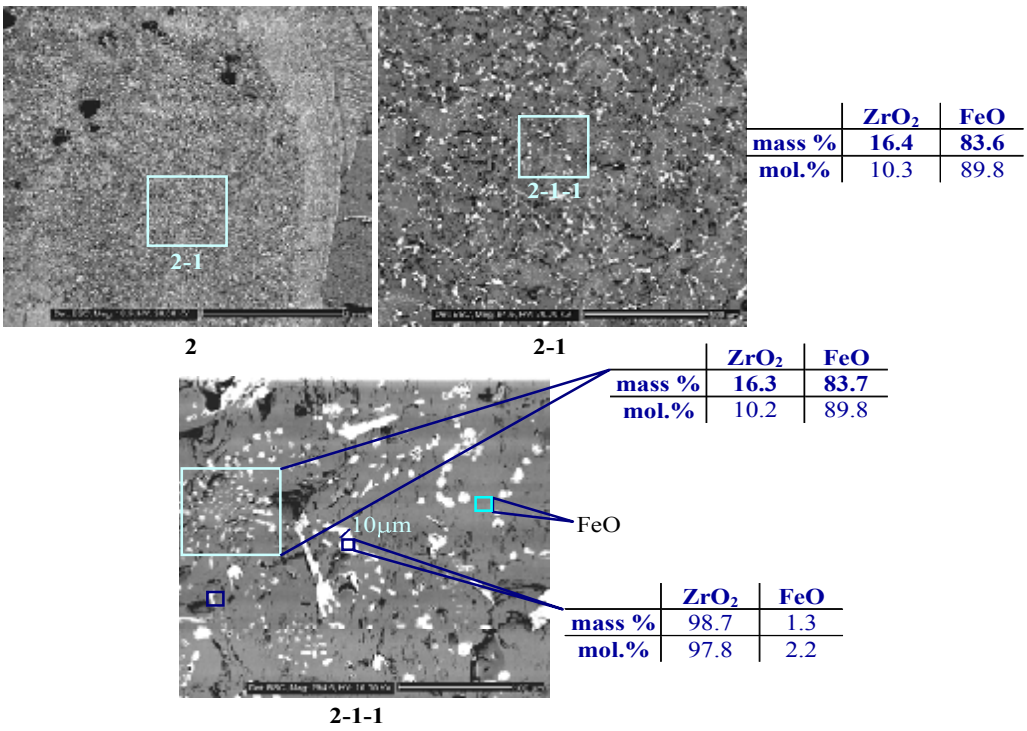

Fig. 2.4. Micrographs of region 2 from the ingot and EDX results

A sample for XRD has been prepared from the eutectic nucleus. Fig.2.5 shows this sample difractogram, from which it follows that the FeO SS in ZrO_2 crystallizes in the monoclinic form. The matter is that the tetr. →monoclinic transition follows the martensite mechanism, i.e., the tetragonal form of zirconia cannot be quenched because of the tetr. →monoclinic transition high rate. That is why only the monoclinic form of zirconia is recorded on difractograms.

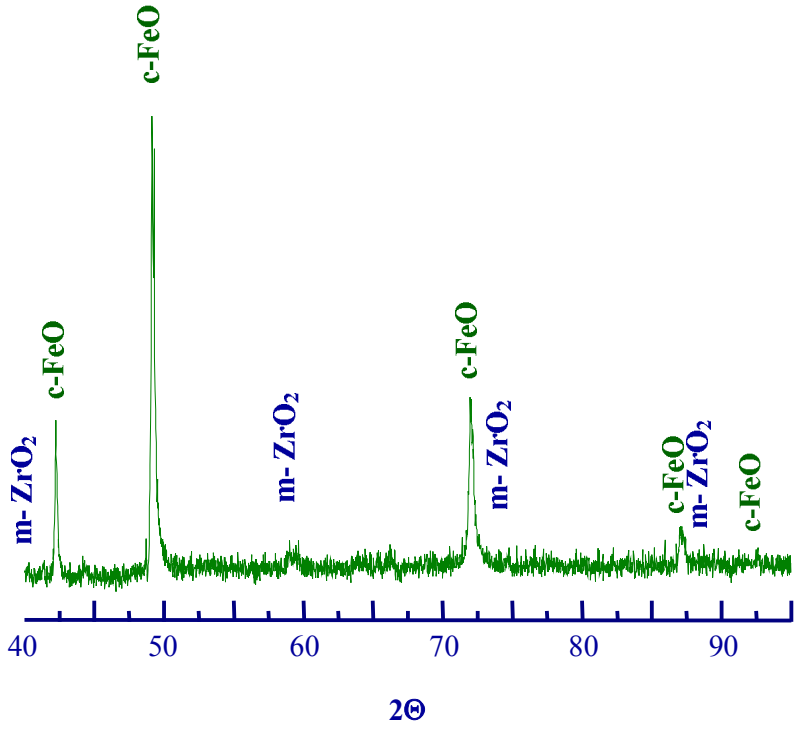

Fig. 2.5. Difractogram of eutectic nucleus sample 2-1-1 (Co-radiation): m-ZrO_2 – monoclinic form of zirconia; c-FeO – cubic form of iron oxide. Marked are only the strongest peaks of C-FeO and m-ZrO_2

The total melt volume was quenched in this test with a water-cooled crystallizer, and therefore the ingot microstructure was studied using pieces chipped from different zones instead of the axial section. Quenching was done at the melt surface temperature of 2120 °C. The results of CORD 4 section studies are given in Figs. 2.6-2.8.

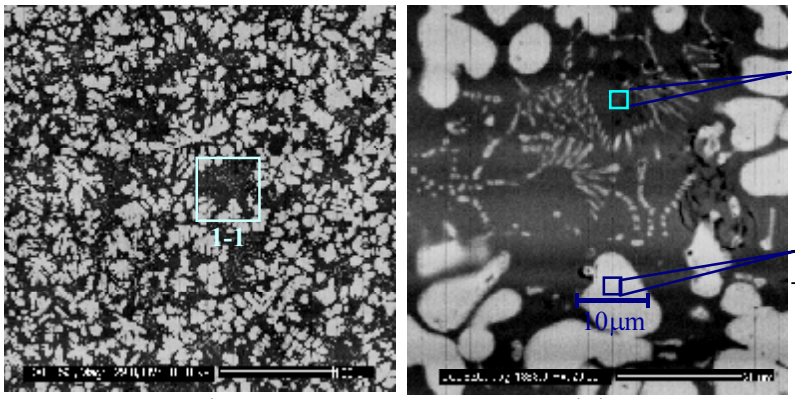

1

	ZrO_2	FeO
mass %	50.8	49.2
mol.%	37.5	62.5

1-1

	ZrO_2	FeO
mass %	93.4	6.6
mol.%	89.1	10.9

Fig. 2.6. Micrographs of CORD 4 sample (quenched melt upper zone) and EDX results

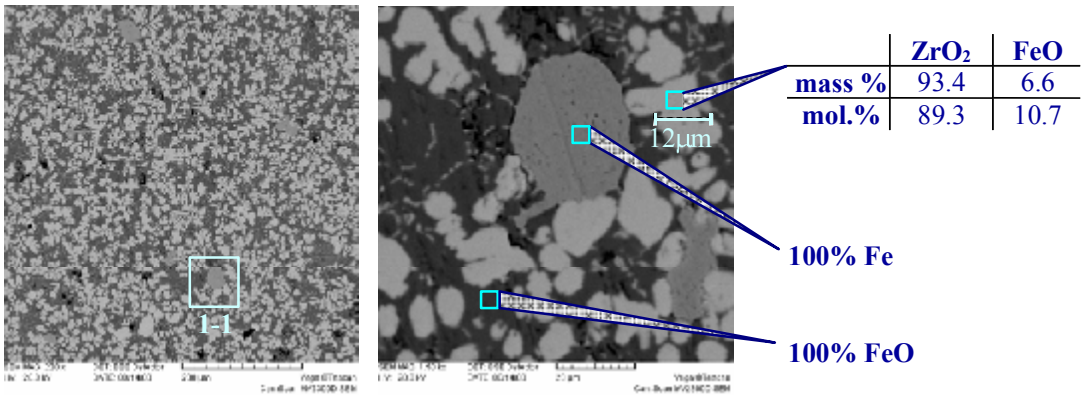

	ZrO_2	FeO
mass %	93.4	6.6
mol.%	89.3	10.7

	ZrO_2	FeO
mass %	50.9	49.1
mol.%	37.7	62.3

Fig. 2.7. Micrographs of sample with CORD 4 composition (quenched melt central zone) and EDX results

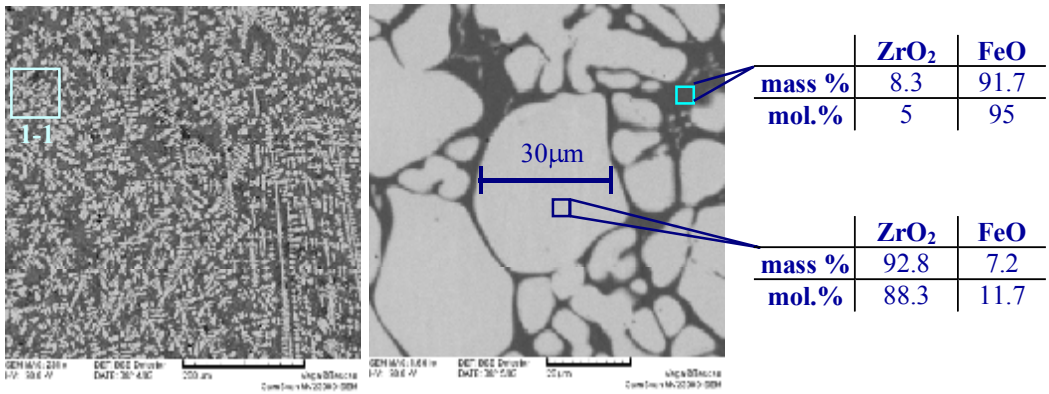

	ZrO_2	FeO
mass %	8.3	91.7
mol.%	5	95

	ZrO_2	FeO
mass %	92.8	7.2
mol.%	88.3	11.7

	ZrO_2	FeO
mass %	46.9	53.1
mol.%	34.0	66.0

Fig. 2.8. Micrographs of sample with CORD 4 composition (quenched melt lower zone) and EDX results

The dendritic, finely dispersed character of the microstructure in all zones indicates to the quenching crystallization. Noteworthy is that free iron was discovered as round droplets only in the ingot central zone. It may be associated with the stratified melt structure when iron was located in the central part of the pool.

In this case, the grains of the FeO SS in ZrO_2 have formed under the nonequilibrium conditions. In addition, a high content of FeO (7.2 mass %) was noted.

For the sake of comparing the melt composition when measuring T_{liq} by VPA IMCC and due to the small amount of the rod sample of the melt, it was used for preparing a section for EDX. The analysis has shown the FeO content to be from 53.7 to 54.2 mass %.

Figs. 2.9 and 2.10 show difractograms of samples from the upper and central zones, from which it follows that the FeO SS in ZrO_2 crystallizes in the cubic form.

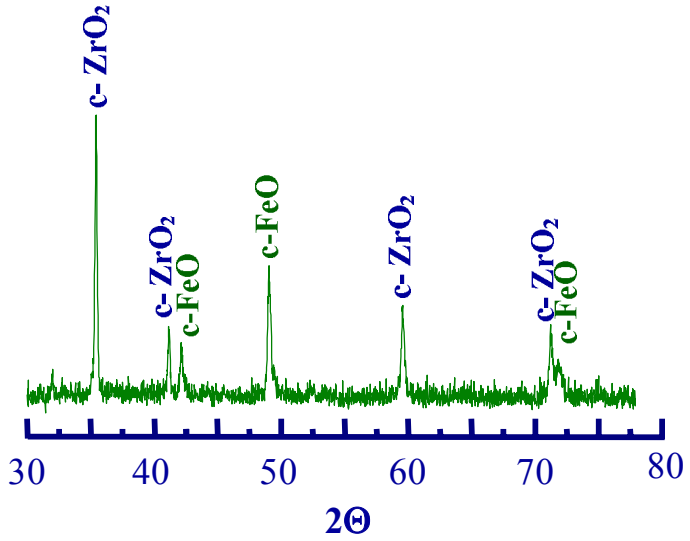

Fig. 2.9. Difractogram of CORD 4 sample (quenched melt upper zone) (Co-radiation): c-ZrO_2 – cubic form of zirconia; c-FeO – cubic form of iron oxide. Marked are only the strongest peaks of c-FeO and c-ZrO_2

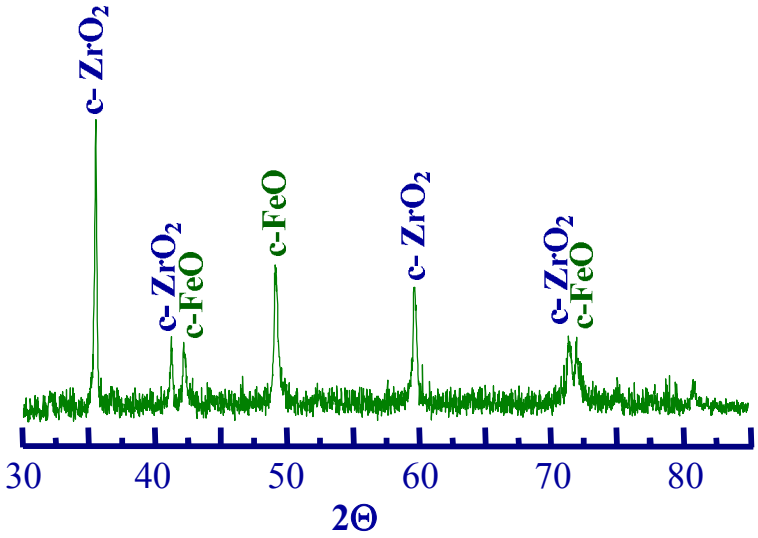

Fig. 2.10. Difractogram of CORD 4 sample (quenched melt central zone) (Co-radiation): c-ZrO_2 – cubic form of zirconia; c-FeO – cubic form of iron oxide. Marked are only the strongest peaks of c-FeO and c-ZrO_2

For a more precise determination of the SS composition, a sample was chipped out from the quenched melt central zone and processed as follows:

- crushed in the Abich mortar and subjected to magnetic separation into the magnetic (~30 mass %) and nonmagnetic (~70 mass %) fractions.

- the magnetic fraction was crushed in the vibratory mill into particles sized < 50 μm;

- the obtained highly dispersed fraction was treated with the concentrated HCl under heating in order to dissolve free FeO;

- the powder was washed with water, dried at 105 °C and screened through a sieve with 40 μm mesh dimension.

The obtained powder was subjected to XRD and XRF.

The difractogram in Fig. 2.11 shows the ZrO_2-based solid solutions in cubic and monoclinic modifications. A calculation of the cubic zirconia parameters has yielded a=5.09±0.04 □, V=132±3 □^{3}. The published data for the stabilized cubic zirconia are as follows: a=5.097±0.07 □, V=132.4±0.5 □^{3} [17, 18].

The c-ZrO_2 / m-ZrO_2 ratio, calculated by the common formula [19]:

$$\frac{c}{m} = \frac{I_{\text{c-ZrO}_2}}{I_{\text{c-ZrO}_2} + I^1_{\text{m-ZrO}_2} + I^2_{\text{m-ZrO}_2}} \cdot 100\%, \qquad (3)$$

where $I_{\text{c-ZrO}_2}$ – intensity of X-ray diffraction maximums of the tetragonal and cubic forms of zirconia; $I^1_{\text{m-ZrO}_2}$ and $I^2_{\text{m-ZrO}_2}$ – intensity of X-ray diffraction maximums of the monoclinic form of zirconia (see Fig. 2.31),

yields the cubic form content in zirconia equal to 70.347%. ($\frac{11572.3}{11572.3 + 3143 + 1734.9} \cdot 100 = 70.347$).

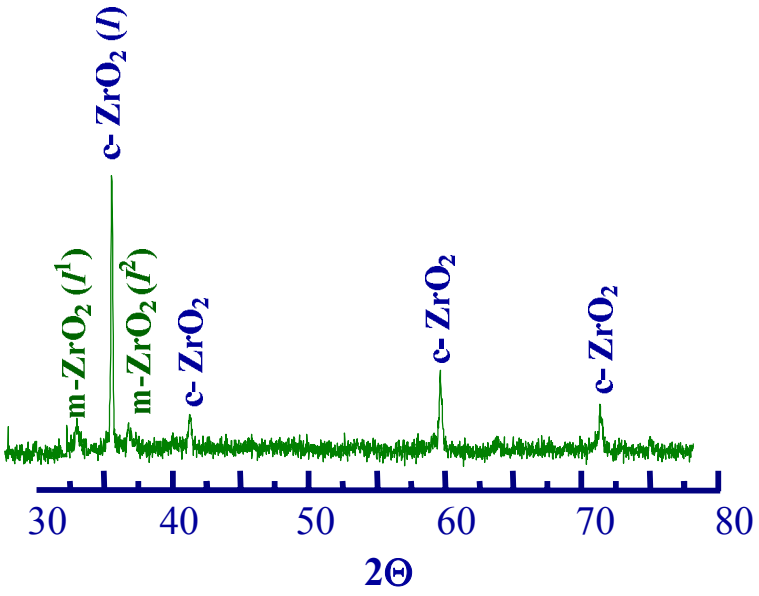

Fig. 2.11. Difractogram of CORD 4 sample after treatment with hydrochloric acid (Co-radiation): c-ZrO_2 – cubic form of zirconia; m-ZrO_2 – monoclinic form of zirconia.

XRF of the washed powder showed the presence of approximately 4.6 mass % iron in terms of FeO. Thus, taking into account the fraction of ZrO_2 cubic form calculated by formula (3) ($95.4 \cdot 0.703 = 67.066$ mass % - cubic form fraction), the ultimate solubility of FeO in ZrO_2 corresponds to 6.419 mass % ($\frac{4.6}{(67.066 + 4.6)} = 6.419\%$).

It should be noted that due to a low content of the SS monoclinic form and low concentration of FeO dissolved in it, all the dissolved FeO was treated as the cubic form in the performed calculations.

Analysis results for the ingot from CORD 5

In CORD 5, as in CORD 4, the total melt volume was quenched in the crucible with the help of a water-cooled crystallizer The results of studying sections from CORD 5 are presented in Figs. 2.12, 2.13 and 2.14.

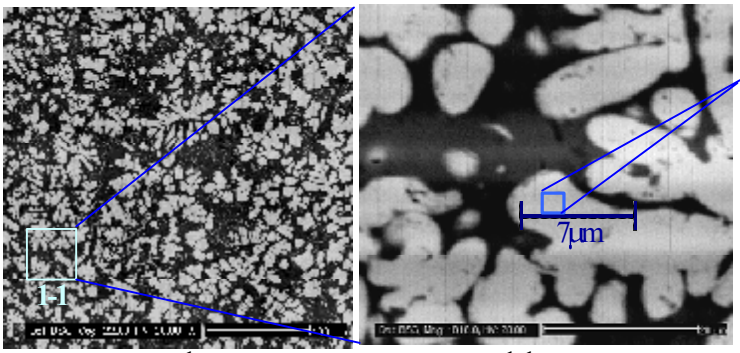

1 1-1

	ZrO	FeO
mass %	94.3	5.7
mol.%	90.5	9.5

	ZrO	FeO
mass %	70.7	29.3
mol.%	58.4	41.6

Fig. 2.12. Micrographs of CORD 5 sample (quenched melt upper zone) and EDX results

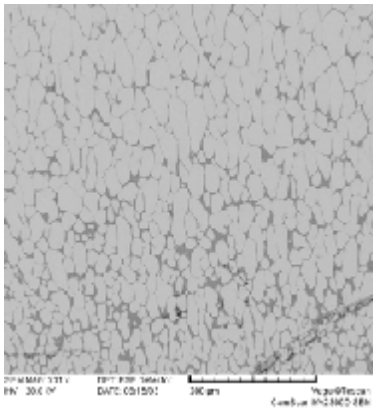

	ZrO_2	FeO
mass %	71.1	28.9
mol.%	58.9	41.1

Fig. 2.13. Micrograph of CORD 5 sample (quenched melt central zone) and EDX results

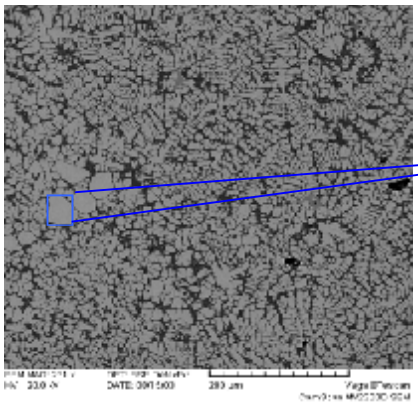

	ZrO_2	FeO
mass %	94.5	5.5
mol.%	90.9	9.1

	ZrO_2	FeO
mass %	70.6	29.4
mol.%	58.3	41.7

Fig. 2.14. Micrograph of CORD 5 sample (quenched melt lower zone) and EDX results

In all three zones the microstructure is of finely dispersed, dendritic type. Unlike in CORD 4, metallic iron is absent from the microstructures. Apparently, the reason is that in this test the melt was quenched at a temperature about 2600 °C, and under these conditions it represented a homogeneous liquid. A more uniform composition in different zones also supposes homogeneity.

In the same way as in CORD 4, the grains of the FeO SS in ZrO2 have formed under the nonequilibrium conditions. FeO solubility in ZrO_2 (cub.) was found to be between 5.5 - 5.7 mass % FeO, i.e., 1.5% mass % lower than in CORD 4. A relative decrease in solubility may be explained by the narrowed area of the cubic SS existence in the high-temperature domain of the diagram.

Like in CORD 4, a section for EDX was prepared from the rod sample of the melt. The analysis showed FeO content to be 31.3 mass %.

Figs.2.15-2.16 show difractograms of the samples prepared from the upper and central zones, from which it follows that the FeO SS in ZrO_2 crystallizes in the cubic form in the same way as in CORD 4.

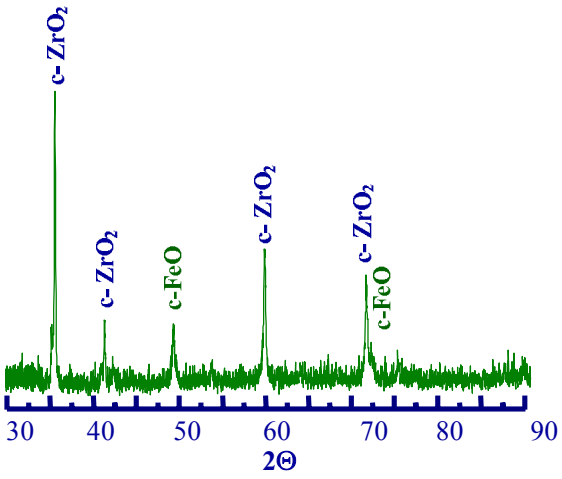

Fig. 2.15. Difractogram of sample with CORD 5 composition (quenched melt upper zone): c-ZrO_2 – cubic form of zirconia; c-FeO – cubic form of iron oxide. Marked are only the strongest peaks of c-FeO and c-ZrO_2

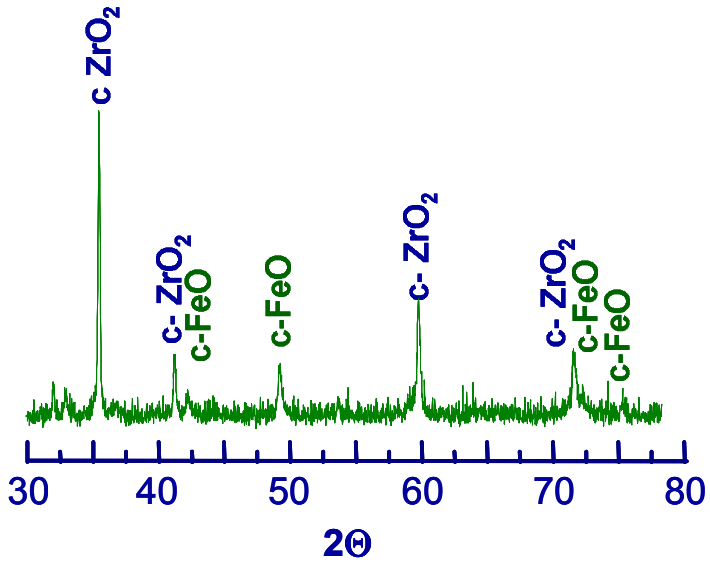

Fig. 2.16. Difractogram of CORD 5 sample (quenched melt central zone): c-ZrO_2 – cubic form of zirconia; c-FeO – cubic form of iron oxide. Marked are only the strongest peaks of c-FeO and c-ZrO_2

Analysis results for the ingot from CORD 9

The CORD2 results have shown a discrepancy between the measured eutectic composition and the work [1] data. Therefore, an additional test was performed. It employed the technique of melt crystallization under the conditions close to equilibrium achieved by shifting the crucible with the melt slowly (at 5-10 mm/h) and continuously relative to the inductor and forming a eutectic nucleus in the ingot upper part.

The charge composition was taken in accordance with the CORD 2 test, i.e., ZrO_2/FeO. = 16.3/ 83.7 mass.%. The diagram of examining the ingot axial section is given in Fig. 2.17. The results of studying the CORD 9 ingot are presented in Figs. 2.17-2.19.

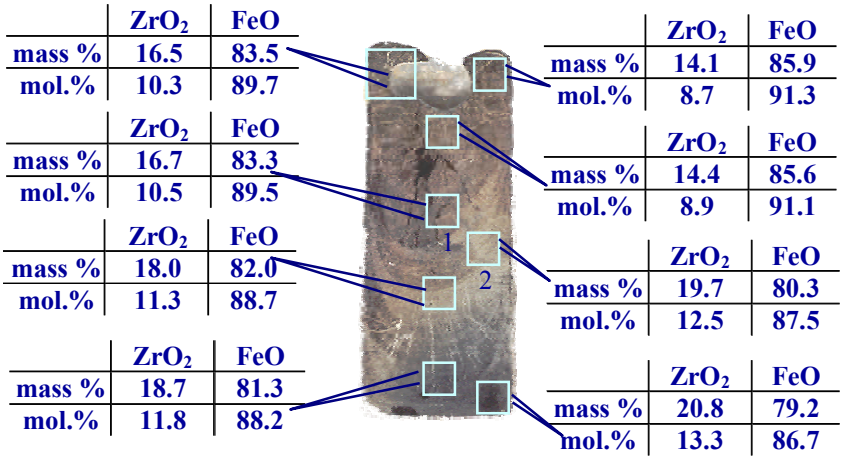

Fig. 2.17. Template from CORD 9 with locations marked for examination and EDX results

The produced ingot is special, as it is the result of almost 6 hours of melt crystallization at shifting the crucible slowly from the inductor zone at 8 mm/h. Therefore, though the ingot structure is heterogeneous and eutectic along almost the entire height, it is nevertheless quite dense, with exception for the shrinkage friability which has formed from the final pool crystallization at the disconnection of heating. This friability is seen in Fig. 2.17 above the

analyzed region 1. It is here, in region 1, that crystallization of the purely eutectic liquid, free from phases of initial crystallization, is most probable. A micrograph of the eutectic region 1 is presented in Fig. 2.18.

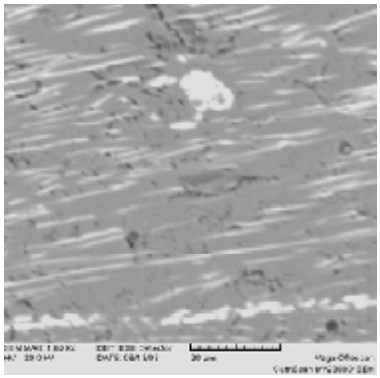

	ZrO_2	FeO
mass %	16.7	83.3
mol.%	10.5	89.5

Fig. 2.18. Micrograph of region 1 and EDX results

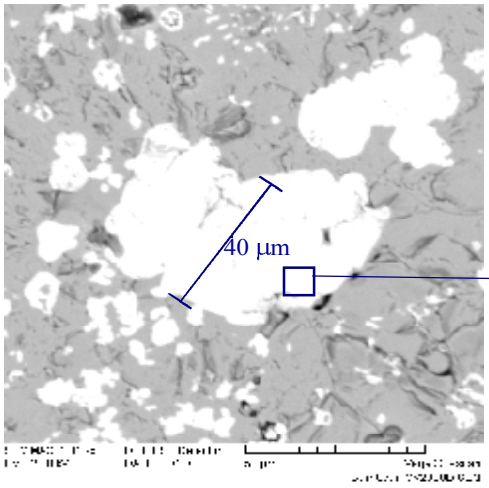

	ZrO_2	FeO
mass %	98.7	1.3
mol.%	97.7	2.3

Fig. 2.19. Micrograph of region 2 and EDX results

Region 2 is characterized by the presence of a large grain of the FeO SS in ZrO_2 which has formed under equilibrium crystallization of the eutectic composition. Therefore, the content of 1.3 mass % FeO in the SS grain may be regarded as the ultimate one for the eutectic temperature.

A sample for XRD has been prepared from the eutectic nucleus. The difractogram in Fig. 2.20 shows that the FeO SS in ZrO_2 crystallizes in the monoclinic form.

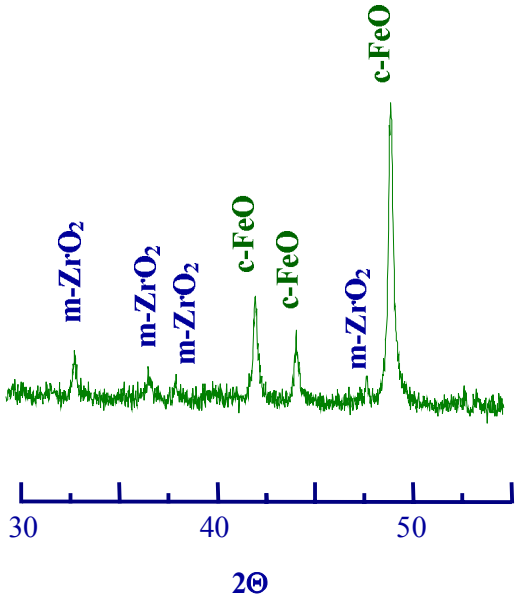

Fig. 2.20. Difractogram of sample from eutectic nucleus of CORD 9 ingot (Co-radiation). Marked are only the strongest peaks of c-FeO and m-ZrO_2

Analysis results for the ingot from CORD 12

Fig. 2.21 shows a micrograph of the characteristic region of the template from CORD 12. Noteworthy are the absence of crystallized drops of free iron, porosity of the FeO phase and a different (in contrast to CORD 2, 4, 5 and 9) type of SS crystallization (FeO-filled cavities observed in dendrites). FeO isolation inside the SS grain indicates to a possible cub. SS $\rightarrow$tetr. SS transition in this region.

FeO solubility in ZrO_2 is also very high (see Tab. 2.8, P1 and P2 points) in comparison to that determined in CORD 4 and CORD 5. The areas of FeO crystallization might have possibly been captured by the microprobe attachment scanning field during P2 examination, and hence the content of FeO content in SS might be overestimated. Also, it may be the influence of a higher (if compared to CORD 2, 4, 5 ,9) oxygen potential of the system, which has little effect on T_{liq}, but may strongly influence (raise) the ultimate solubility of iron oxide in ZrO_2 and affect (decrease) the temperature of polymorphous cub. SS $\rightarrow$tetr. SS transition.

It also should be noted that the melt was naturally chilled down from 1900°C and the SS grains formed during the nonequilibrium crystallization.

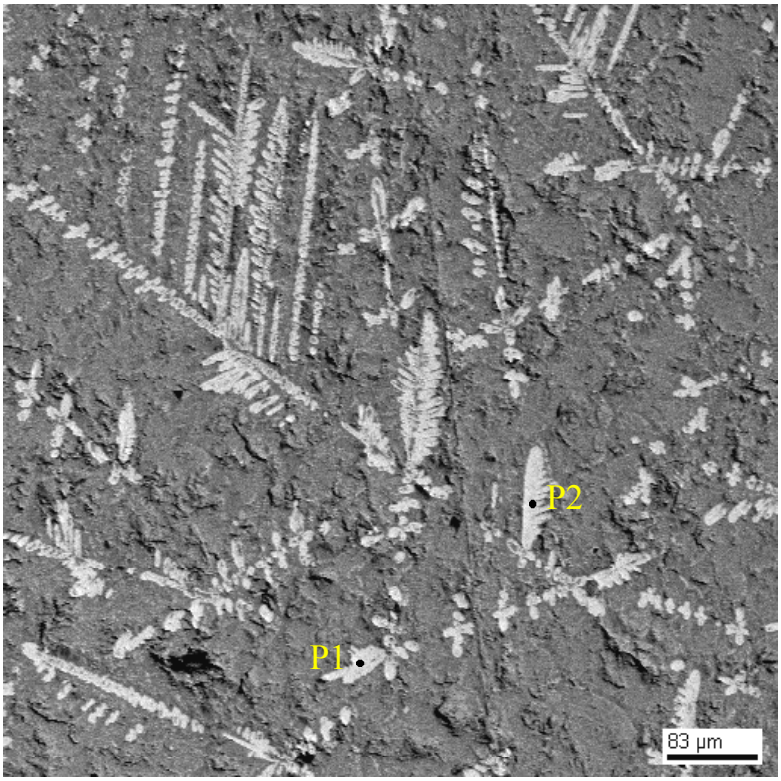

Fig. 2.21. Micrograph of characteristic region of CORD 12 template

Table 2.8. EDX results for characteristic region of CORD 12 template

No.		ZrO_2	FeO
SQ	mass %	29.85	70.15
	mol.%	19.88	80.12
P1	mass %	89.33	10.67
	mol.%	83.00	17.00
P2	mass %	85.23	14.77
	mol.%	77.09	22.91

Analysis results for the ingot from CORD 24

The diagram of examining the ingot axial section is given in Fig. 2.21. The results of studying the CORD 24 ingot are presented in Figs. 2.22-2.52.

Among peculiarities of this test is the growing of an equilibrium crystallization layer by drawing the ingot from the inductor at 8-10 mm/h within 1 hour. Thus, the ingot peripheral area represents a monophase layer of ZrO_2 with FeO dissolved in it.

The bulk composition of the ingot central part is depleted (in this case, at the expense of growing the equilibrium crystallization layer) in zirconia in comparison with the ZrO_2 mass in the initial charge (Tab. 2.8, SQ region; Tab. 2.9, SQ3 region; Tab. 2.10, SQ1 region).

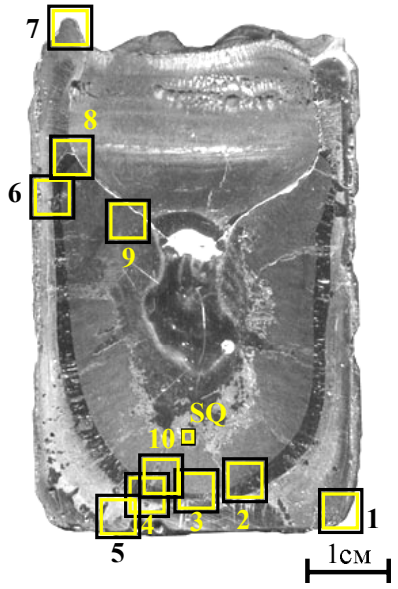

Fig. 2.21. Template with regions marked for analysis. (Dark peripheral layer is the monophase layer of crystals of FeO cubic SS in ZrO_2)

Table 2.8. EDX results for SQ region

No.		ZrO_2	FeO
SQ	mass %	46.75	53.25
	mol.%	33.86	66.14

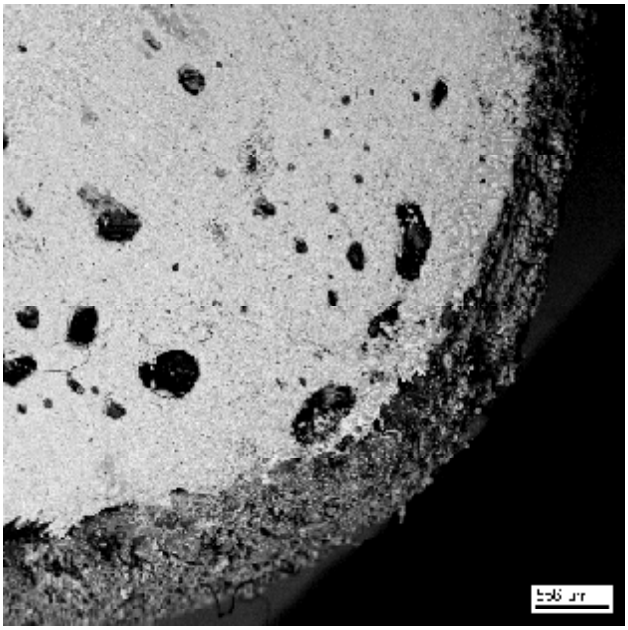

Fig. 2.22. Micrograph of region 1

Region 1 in Fig. 2.22 shows high porosity of the quenched melt. Regions 2, 3 and 4 are of interest because they include a monophase layer of SS crystals and demonstrate a clearly outlined crystallization front.

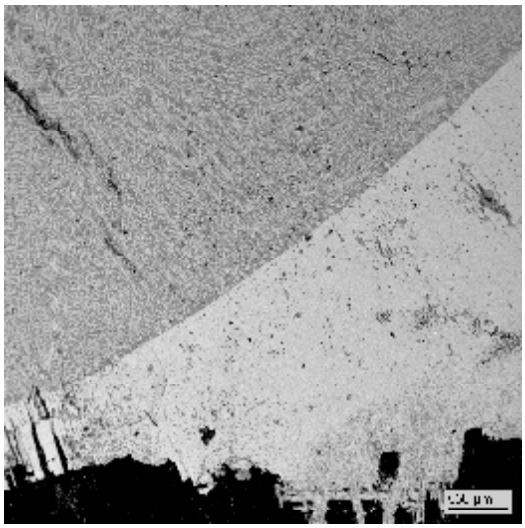

Fig. 2.23. Micrograph of region 2

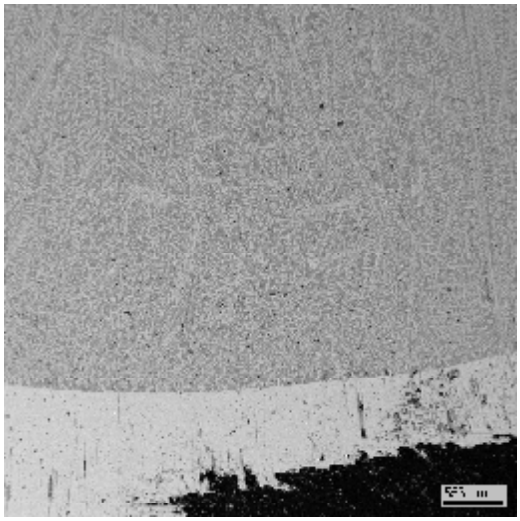

Fig. 2.24. Micrograph of region 3

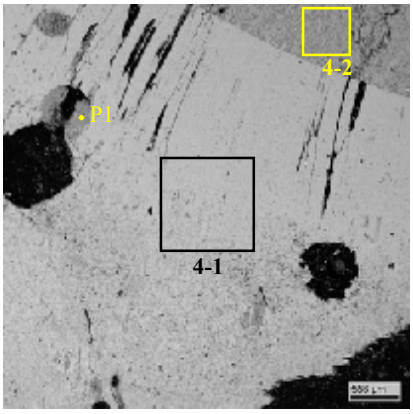

4

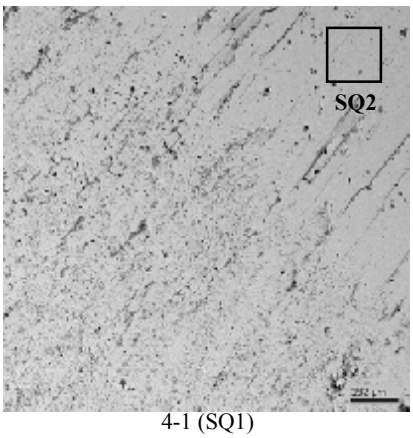

4-1 (SQ1)

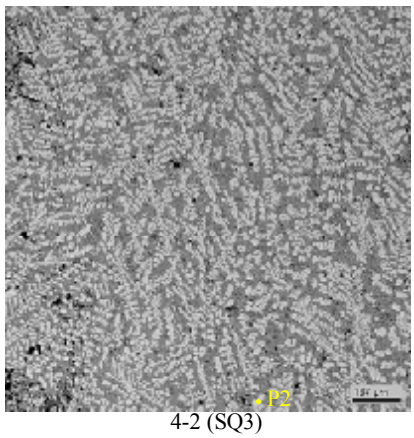

4-2 (SQ3)

Fig. 2.25. Micrographs of region 4

Table 2.9. EDX results for region 4

No.		ZrO_2	FeO
SQ1	mass %	88.10	11.90
	mol.%	81.19	18.81
SQ2	mass %	92.02	7.98
	mol.%	87.05	12.95
SQ3	mass %	44.18	55.82
	mol.%	31.58	68.42
P1	mass %	-	100
	mol.%	-	100
P2	mass %	90.35	9.65
	mol.%	84.52	15.48

The solubility limit of iron oxide in this test is reasonable to determine in the equilibrium crystallization zone. The analysis of FeO solubility in this zone has shown it to be 7.98 mass % (Fig. 2.25; Tab. 2.9, SQ2 region). Therefore, this value may be taken as the solubility limit in the region which composition corresponds to that of bulk melt that has crystallized near the front, i.e., 44.18 mass % ZrO_2 (Fig. 2.25; Tab. 2.9, SQ3 region).

It should be noted that P2 point in the same Fig. 2.25 represents the identical ZrO_2-based SS. However, these crystals are components of a heterogeneous structure of the final melt that has crystallized after the disconnection of heating. As the size of crystals is small, their composition is not representative and was not taken into consideration.

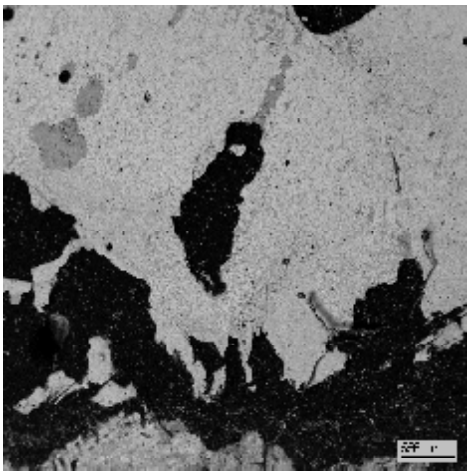

Fig. 2.26. Micrograph of region 5

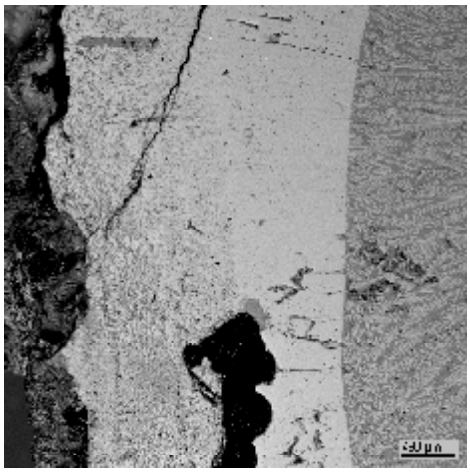

Fig. 2.27. Micrograph of region 6

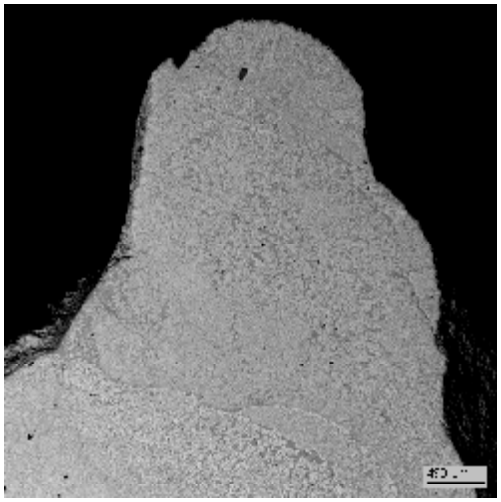

Fig. 2.28. Micrograph of region 7

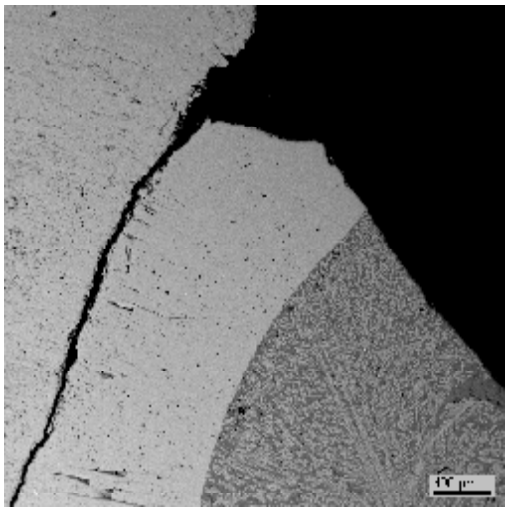

Fig. 2.29. Micrograph of region 8

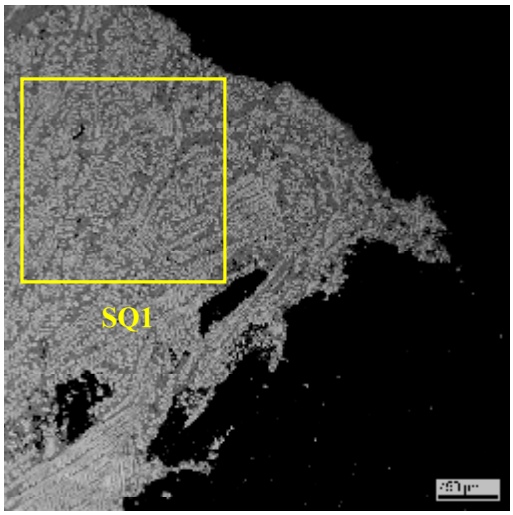

Fig. 2.30. Micrograph of region 9

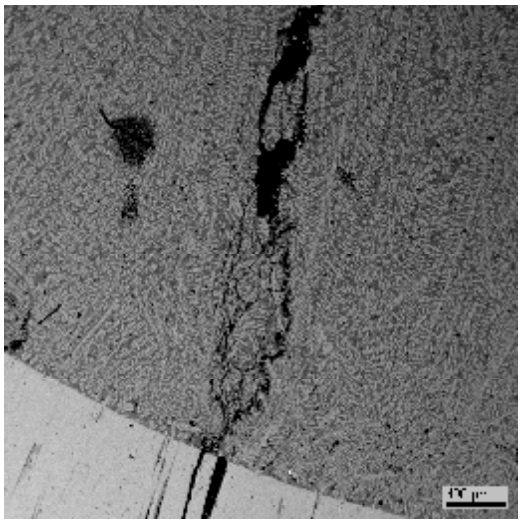

Fig. 2.31. Micrograph of region 10

Table 2.10. EDX results for region 9

No.		ZrO_2	FeO
SQ1	mass %	48.05	51.95
	mol.%	35.03	64.97

The microstructure micrographs (Figs. 2.26 – 2.31) present the pictures of equilibrium and nonequilibrium crystallization in regions 5 – 10. EDX of the corresponding structures yields similar results.

Analysis results for the ingot from CORD 29 A

The isolation of FeO inside the SS grains was recorded when examining the template from CORD 12. In order to test the hypothesized cub. SS →tetr. SS transition with the concomitant liquid ferrous oxide isolation at a temperature around T_{liq} for the composition of CORD 12 (approximately 1800 °C), CORD 29A was carried out to synthesize a high-temperature FeO cubic SS in ZrO_2. The synthesis was aimed at obtaining a quenched structure, preferably throughout the ingot volume, i.e., quenching the cubic SS or a transitional 'cub. SS + tetr. SS' two-phase structure. The samples prepared from the ingot further underwent the following thermal treatment:

- Rapid heating and annealing at 1850 °C in the Galakhov microfurnace resulting in a 'cub. SS + tetr SS' two-phase structure;
- Slow temperature reduction to 1700 °C;
- Recording of the temperature of liquid phase appearance at the cub. SS →tetr. SS transition;
- Quenching.

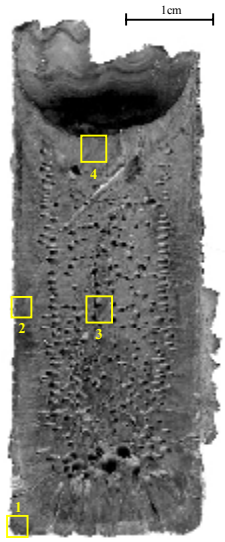

Fig. 2.32. Template from CORD 29A with regions marked for analysis

The diagram of examining the ingot axial section is given in Fig. 2.32. The results of SEM/EDX analysis of the CORD 29A ingot are presented in Figs. 2.33-2.36.

The scattered porosity, clearly visible in Fig 2.32, is the result of the melt superheating and high crystallization rate. This is an indication of the rapid melt chilling and obtaining a quenched structure at the ingot periphery.

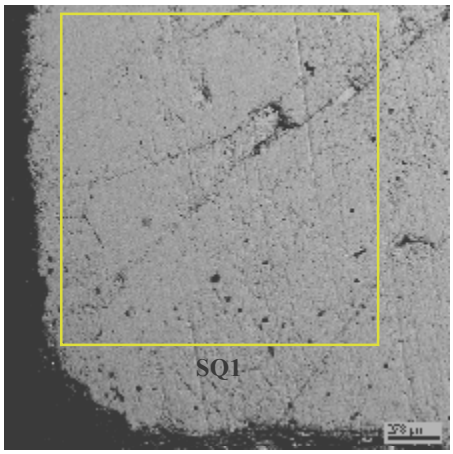

Fig. 2.33. Micrograph of region 1

Table 2.11. EDX results for SQ-1 region

No.		ZrO_2	FeO
SQ-1	mass %	97.95	2.06
	mol.%	96.53	3.47

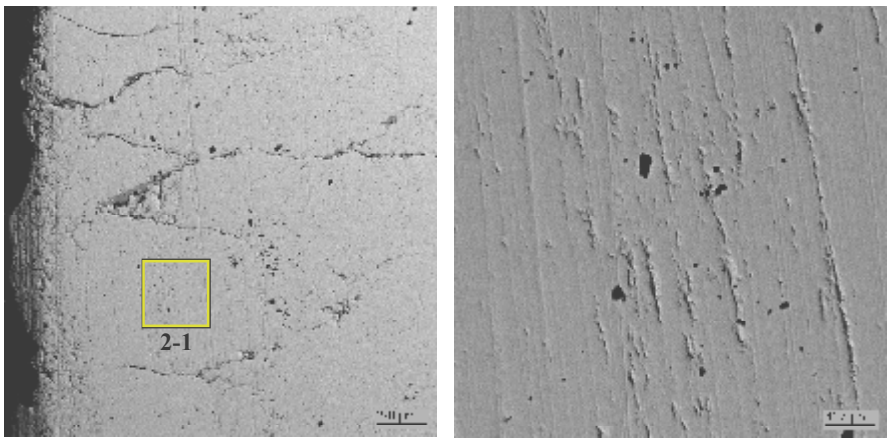

2 2-1(SQ1)

Fig. 2.34. Micrographs of region 2

Table 2.12. EDX results for region 2-1

No.		ZrO_2	FeO
SQ1	mass %	97.14	2.86
	mol.%	95.19	4.81

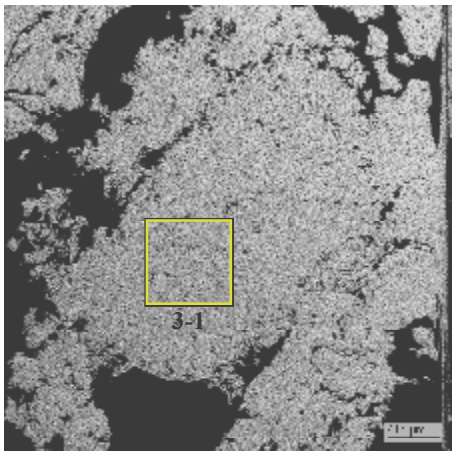

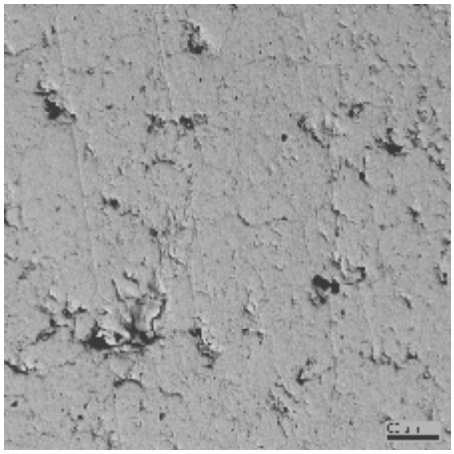

3 3-1(SQ1)

Fig. 2.35. Micrographs of region 3

Table 2.13. EDX results for region 3-1

No.		ZrO_2	FeO
SQ1	mass %	93.52	6.48
	mol.%	89.38	10.62

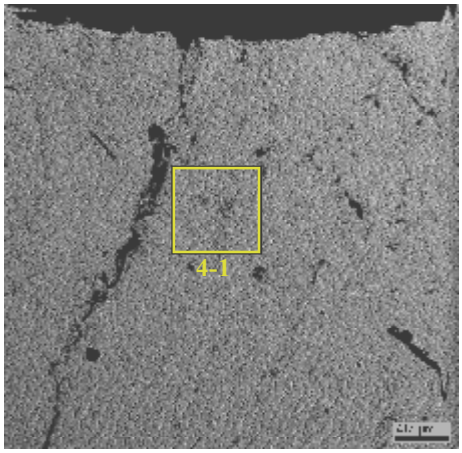

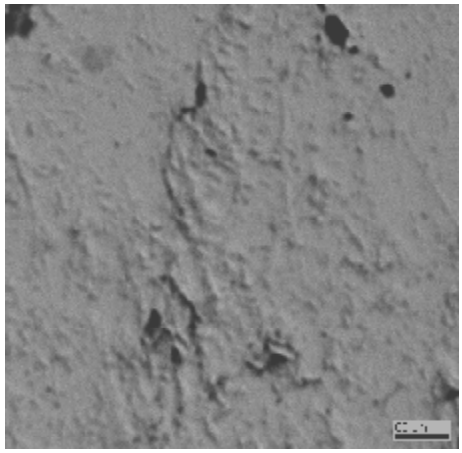

4 4-1(SQ1)

Fig. 2.36. Micrographs of region 4

Table 2.14. EDX results for region 4-1

No.		ZrO_2	FeO
SQ1	mass %	94.50	5.50
	mol.%	90.92	9.08

A comparison of compositions from different parts of the ingot shows that throughout its volume an SS with FeO content in ZrO_2 ranging from 2.06 to 6.4 mass % has been obtained.

The solid solutions were not subjected to XRD.

2.4.5. Generalization of the VPA IMCC results

Figures 2.37 -2.44 and Tab. 2.15 contain the processed and generalized data obtained in the course of studying the ZrO_2-FeO system by VPA IMCC. The figures show thermogram fragments with inserted video frames of the melt surface at the instant of T_{liq} measurement. The data from CORD 1 and 3 are not given, as these tests had to be terminated due to technological reasons.

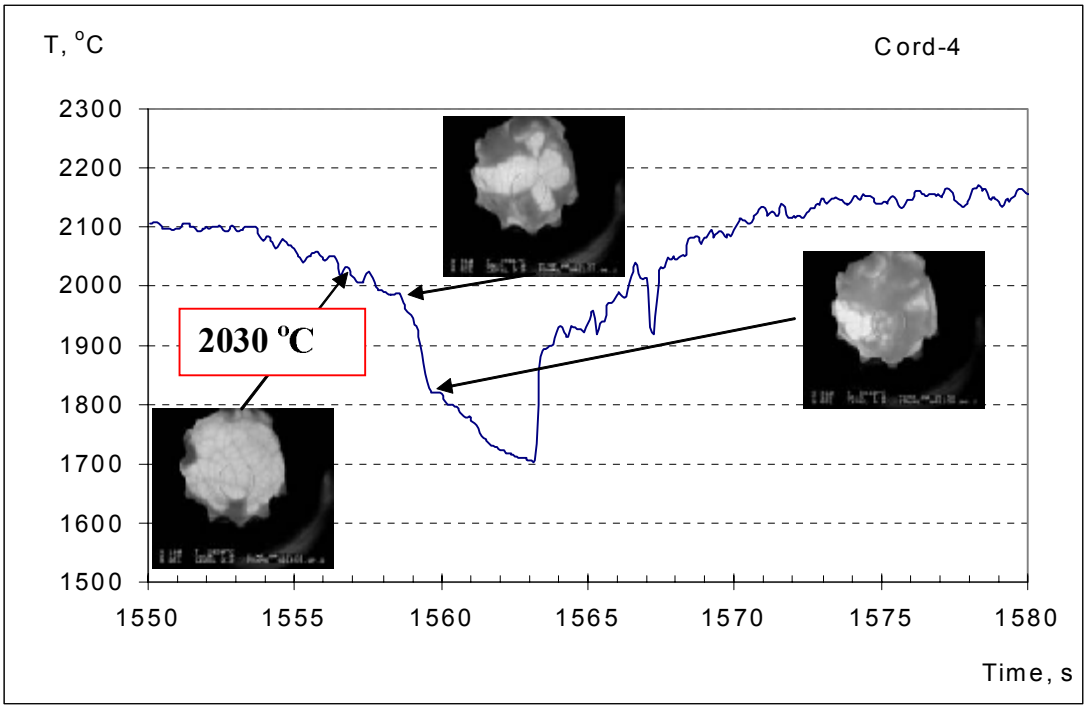

Fig. 2.37. Thermogram fragment from CORD 4 and video frames of melt surface

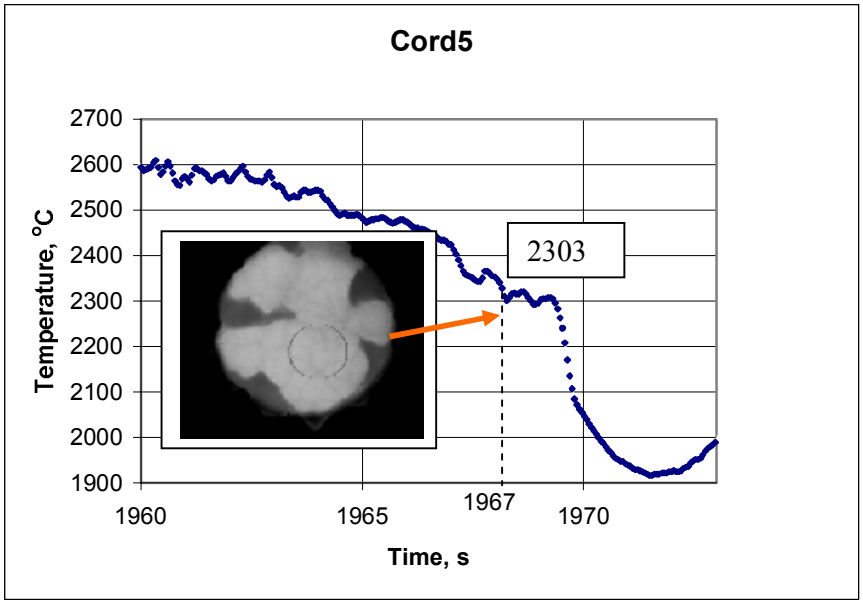

Fig. 2.38. Thermogram fragment from CORD 5 and video frame of melt surface

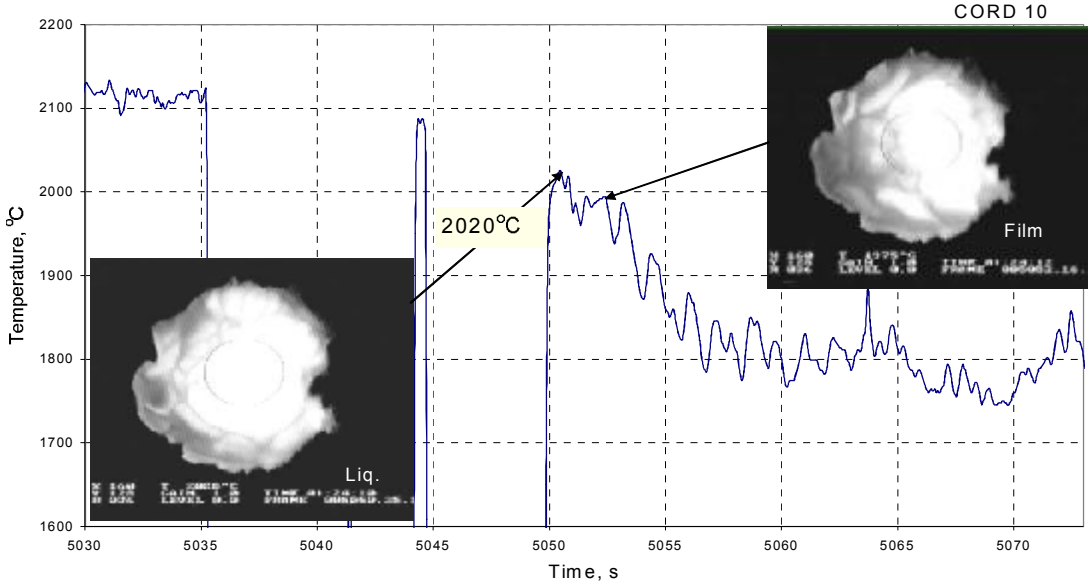

Fig. 2.39. Thermogram fragment from CORD 10 and video frames of melt surface. (Gaps in thermogram are due to accidental shielding of pyrometer lens with the operator's hand)

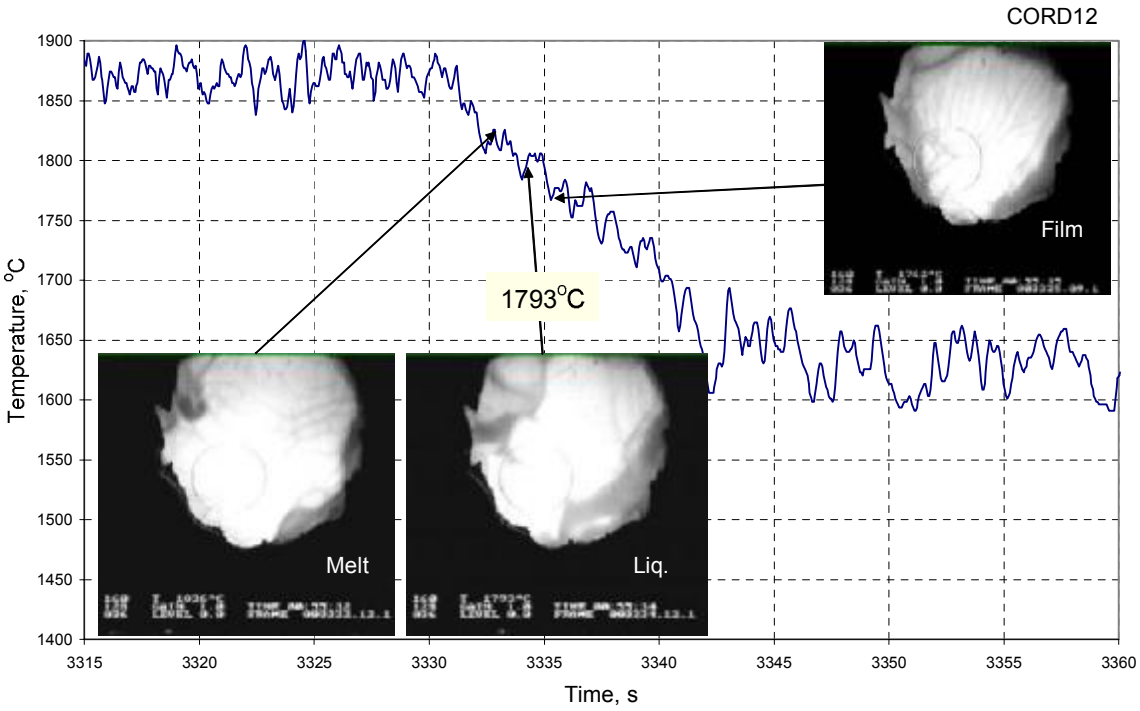

Fig. 2.40. Thermogram fragment from CORD 12 and video frames of melt surface

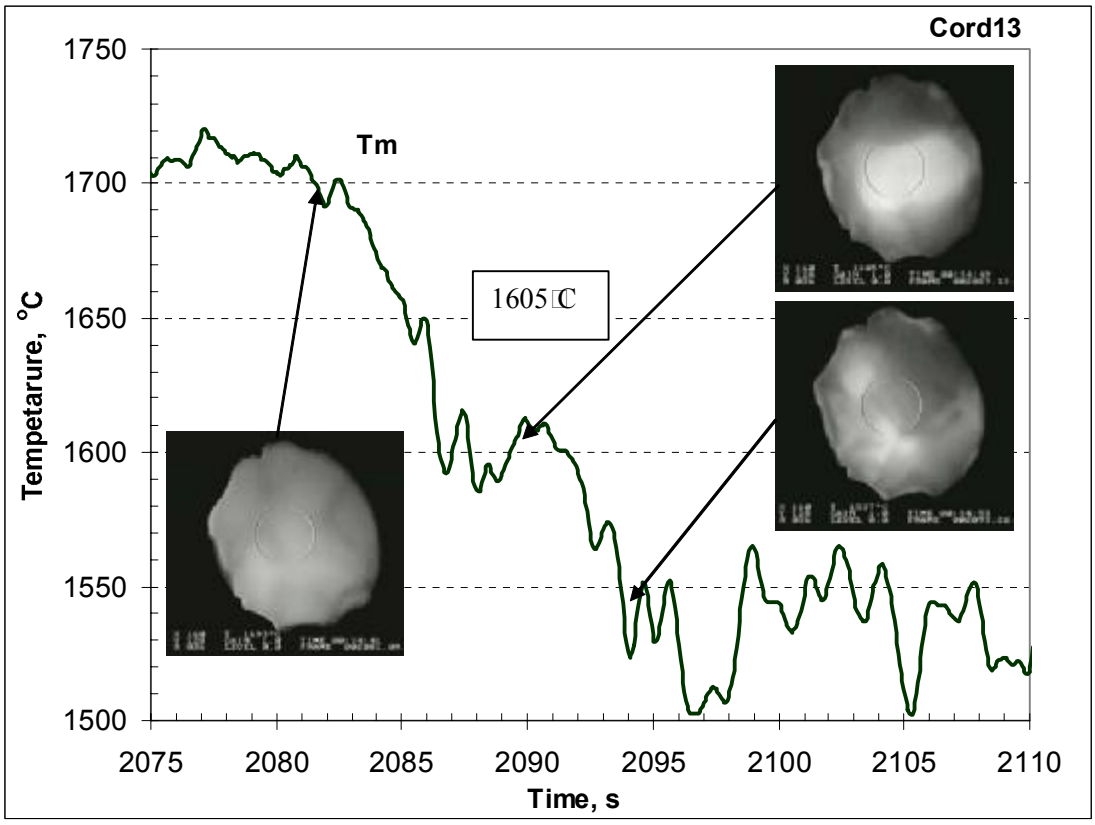

Fig. 2.41. Thermogram fragment from CORD 13 and video frames of melt surface

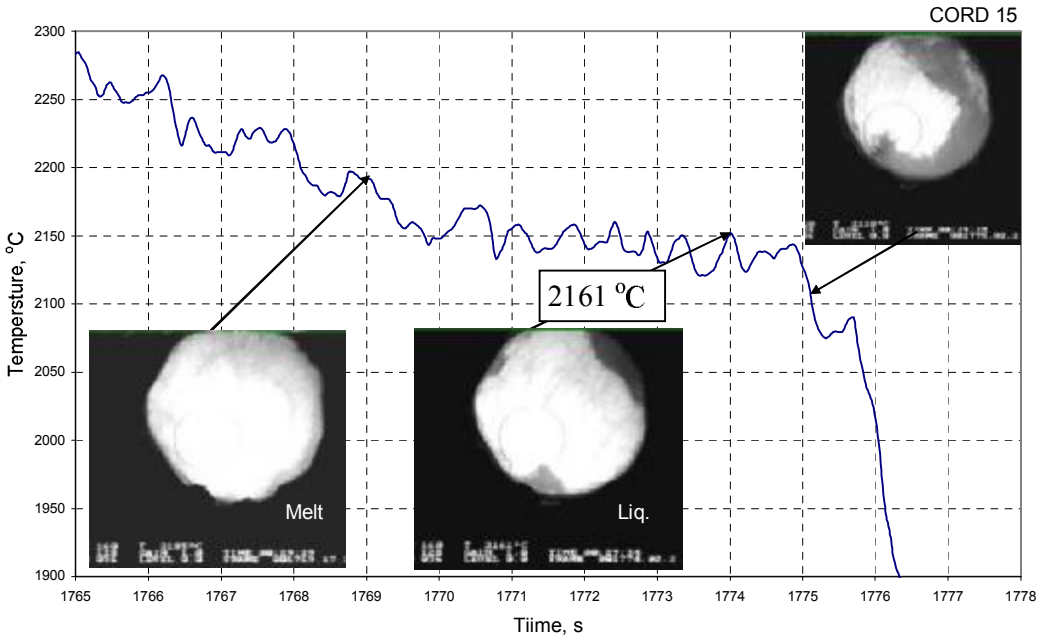

Fig. 2.42. Thermogram fragment from CORD 15 and video frames of melt surface

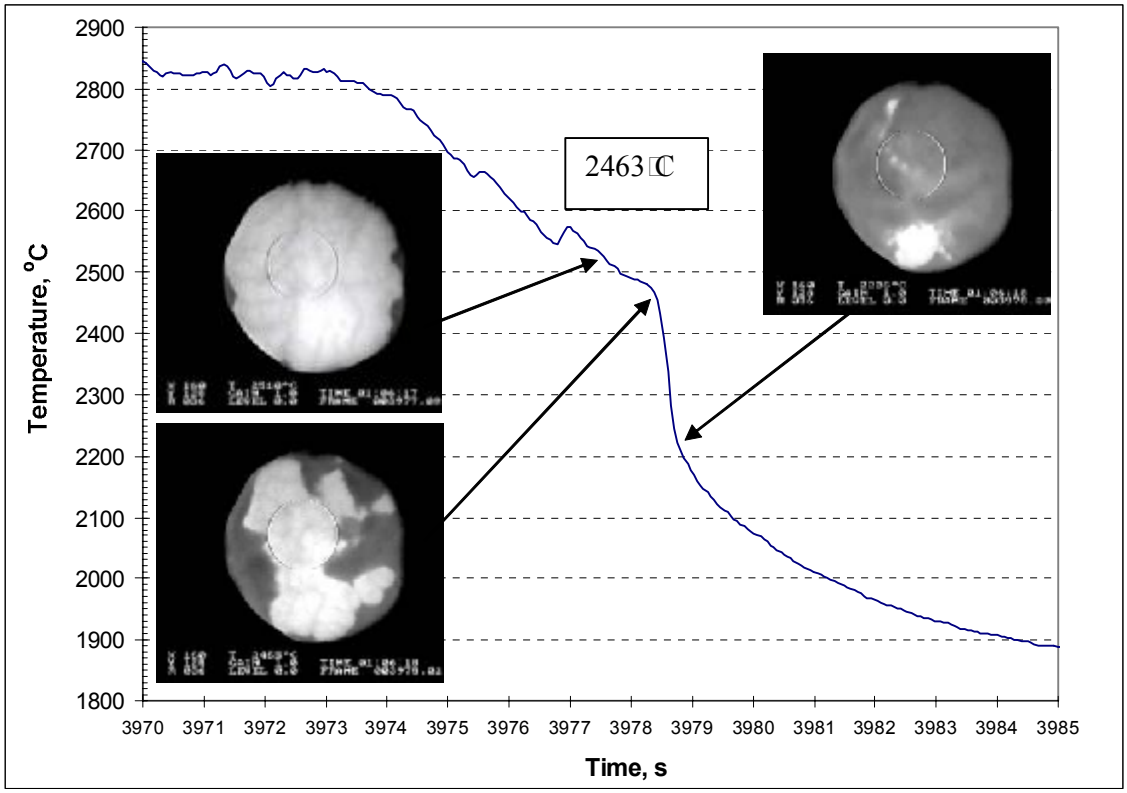

Fig. 2.43. Thermogram fragment from CORD 16 and video frames of melt surface

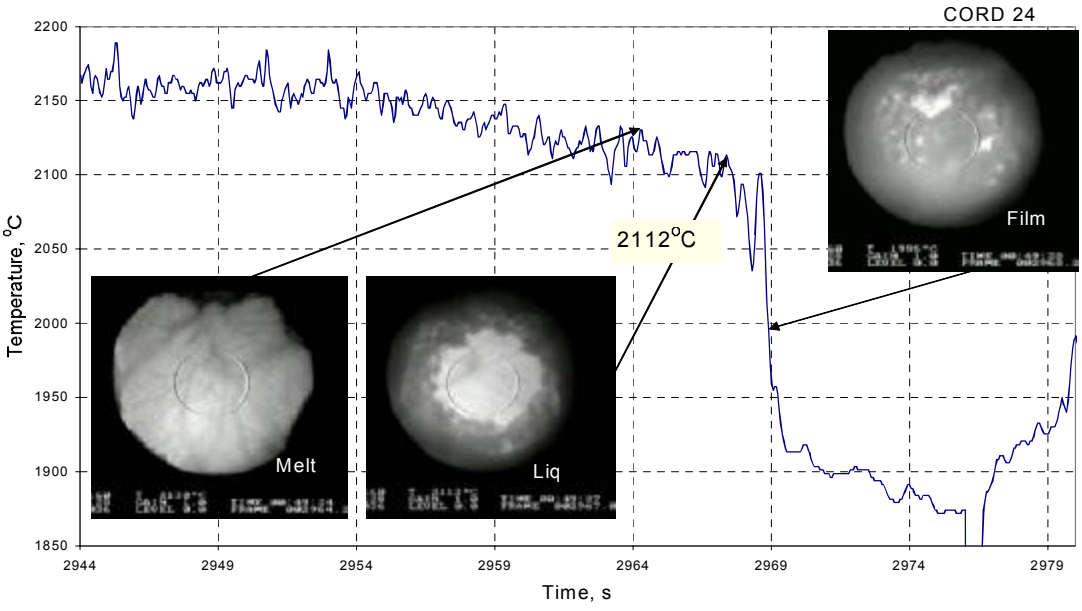

Fig. 2.44. Thermogram fragment from CORD 24 and video frames of melt surface

Table 2.15. VPA IMCC results from tests with the ZrO_2-FeO system

CORD #	ZrO_2, mass %	FeO, mass %	T_{liq}, °C
13	22.6	77.4	1605
12	31.8	68.2	1793
4	46.0	54.0	2030
10	46.6	53.5	2020
24	55.4	44.6	2112
15	60.2	41.8	2161
5	68.7	31.3	2300
16	84.5	19.1	2463

Melt compositions in this Table are given in accordance with the results of chemical and EDX analyses of samples taken from the melts, see Tab 2.4.

3. T_{liq} measurements in the Galakhov microfurnace

For T_{liq} measurements in the Galakhov microfurnace, samples (scales) were prepared from both the melt samples taken in the course of CORD tests and ingots of the crystallized melt. Samples' composition was determined from the EDX results.

CORD2

Samples for the analysis were prepared from region 1 and the eutectic region 2 (Fig. 2.2). A study of the samples from region 1 (Fig. 2.2) in the Galakhov microfurnace has yielded T_{sol} = 1351 °C and T_{liq} = 1353 °C (Fig. 3.1).

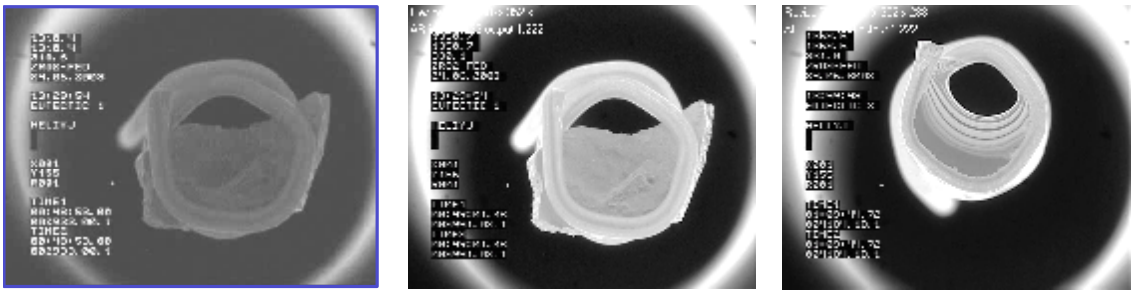

1310°C 1350.7°C 1352.5°C

Technical details, including the sample temperature, is pasted in frames on the left side
Fig. 3.1. View of sample in holder during VPA in the Galakhov microfurnace.

A study of the eutectic region 2 in the Galakhov microfurnace has shown T_{sol} to be equal to 1344 °C (Fig. 3.2)

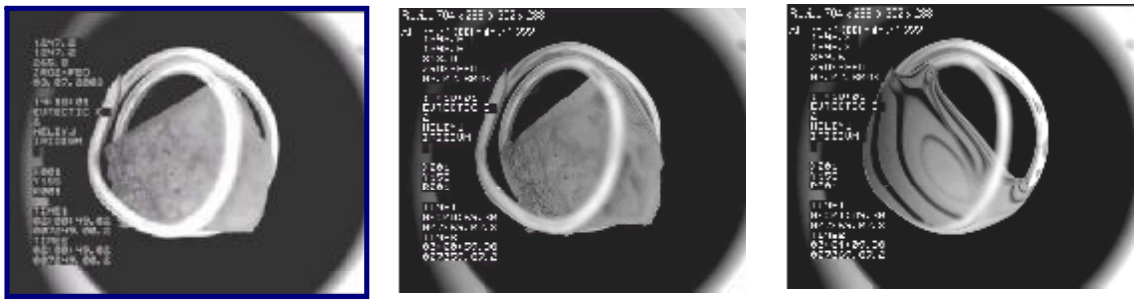

1247°C 1343.5°C 1445.2°C

Fig. 3.2. View of sample in the iridium holder during VPA in the Galakhov microfurnace CORD4

Samples for the analysis were prepared from the central zone of the quenched composition (Fig.2.7).

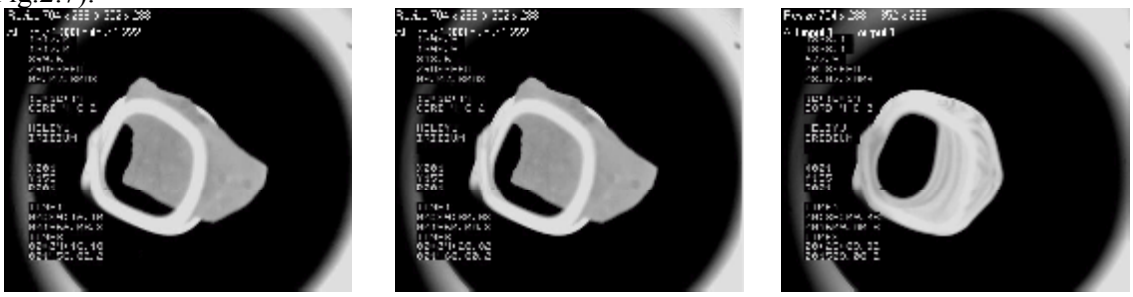

1317°C 1342.4°C 1832.1°C

Fig. 3.3. View of sample in the iridium holder during VPA in the Galakhov microfurnace

A study of the samples in the Galakhov microfurnace has yielded T_{sol} = 1342 °C and T_{liq} = 1832 °C (Fig. 3.1).

CORD5

Samples for the analysis were prepared from the central zone of the quenched composition (Fig.2.13).

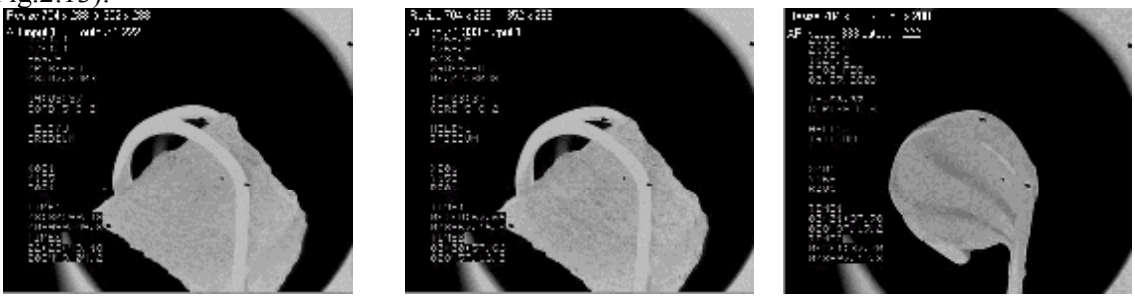

1721.1°C 1758.5°C (active spreading start) 2138.4°C

Fig. 3.4. View of sample in the iridium holder during VPA in the Galakhov microfurnace

The analysis in the Galakhov microfurnace yielded $T_{liq.}$= 2138 °C, which is 200 K lower than that determined by VPA. It should be noted that the last reference point for the Galakhov microfurnace calibration was corundum (melting point = 2054 °C). Above this point temperature values were extrapolated. The present furnace configuration prohibits calibration using a higher-temperature point (e.g., erbium oxide, 2418°C), therefore the results of measurements above 2050 °C may be underrated. Besides, deficiency of the liquid phase in the analyzed region made it impossible to determine T_{sol} for the sample.

Good active wetting of the holder material with the melt and its spreading are characteristic of all samples of the system. To check the presence of the solid phase in the spread melt, it was decided to quench the melt in the next test and examine it by SEM/EDX for the availability of relict (unfused) grains.

The 2nd possible reason of underrating T_{liq} measured by the Galakhov method is the discrepancy between the composition of scales selected from different samples and the average melt composition. That is why in further tests the measurements in the Galakhov microfurnace were followed by SEM/EDX of the samples quenched at dumping them from the furnace hot zone on a cold surface.

CORD24

In this test several samples were taken from the melt at a fixed temperature in order to check data reproducibility. Fig. 3.5 shows SEM/EDX results for a scale from the rod sample No.1 before measurements in the microfurnace, and Fig. 3.6 shows analysis of a scale from the same sample, but after quenching from T_{liq} = 1930°C measured in the microfurnace. Noteworthy is a difference in microstructures. Before the analysis, the structure was dendritic and finely dispersed, while after it enlarged SS grains and changes in their shape are visible. The EDX analysis has also shown the presence of tungsten oxide in the samples, apparently resulting from its oxidation and evaporation from the heater. Tungsten oxide (WO_3) melting temperature is 1474 °C [18]. This also may influence the measurement results.

Fig. 3.7 shows SEM/EDX analysis of a scale from the rod sample No.2, where a significant amount of tungsten oxide was also found. The measured T_{liq} was 1963 °C.

Figs. 3.8, 3.9 and 3.10 contain SEM/EDX results for scales from the sample No.3 (taken with a spoon) before measurements in the microfurnace and after (i.e., after quenching from different temperatures), respectively. Figs. 3.8 and 3.9-3.10 show the microstructure before and after the analysis, respectively. Tungsten oxide was also found in the samples by EDX. Scales quenching from different temperatures (Figs. 3.9, 3.10) resulted in different microstructures. A SEM image (Fig. 3.10) shows the intact initial microstructure. The measured T_{liq} was between 1960-1965 °C.

The SEM/EDX results cannot definitely prove the absence of relict grains, in other words, the complete sample melting at T_{liq} values obtained by the Galakhov method.

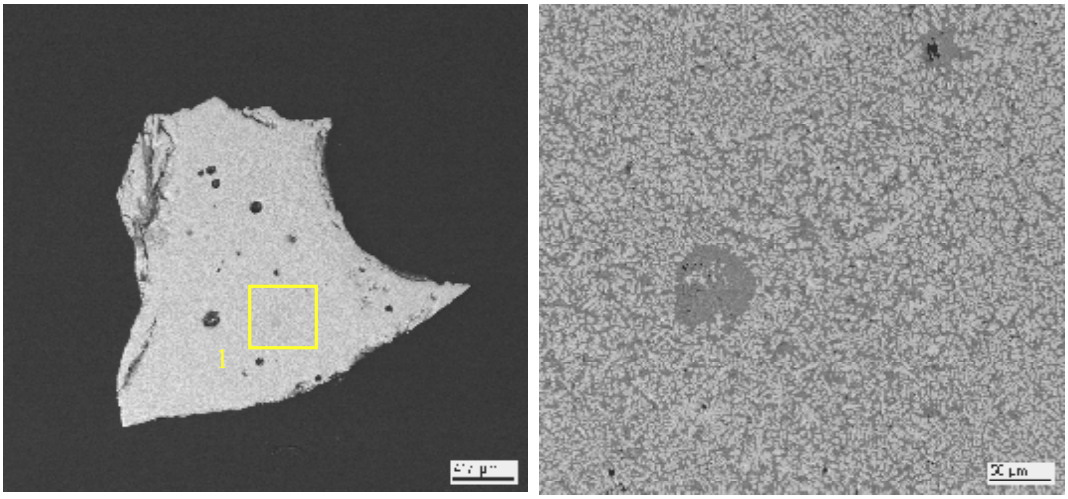

Fig. 3.5. Micrographs of scale from rod sample No. 1 before the microfurnace test

Table 3.1. EDX results for a scale from rod sample No.1 before the microfurnace test

No.		ZrO_2	FeO
SQ1	mass %	53.44	46.56
	mol.%	39.90	60.10

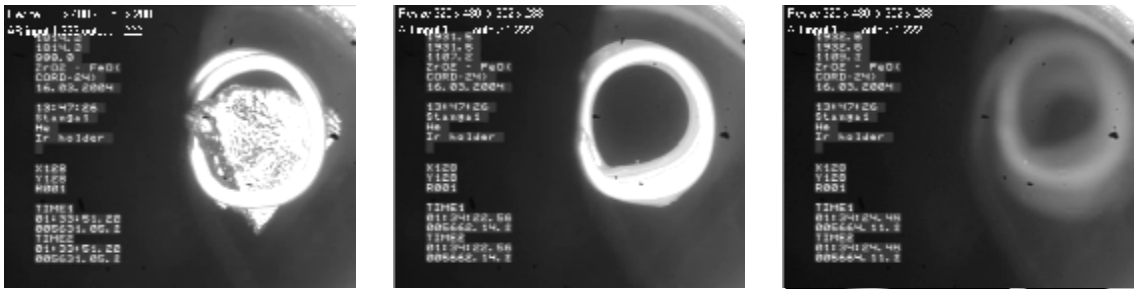

1814.2°C 1931.5°C 1932.8°C (quenching)

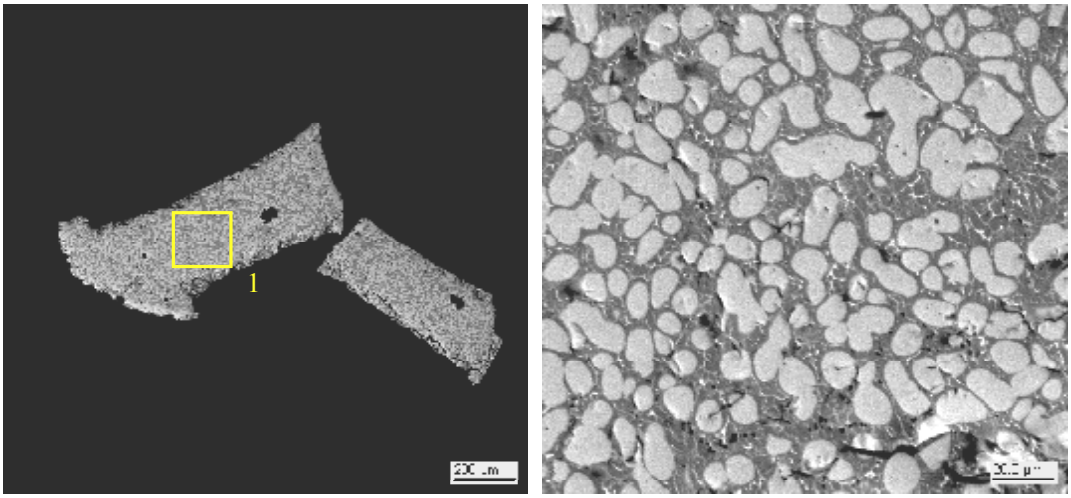

1 (SQ1)

Fig. 3.6. Melting in the microfurnace and micrographs of scale from rod sample No. 1 after quenching

Table 3.2. EDX results for rod sample No.1 after quenching

No.		ZrO_2	FeO	WO_3
SQ1	mass %	56.43	41.96	1.61
	mol.%	43.47	55.87	0.66

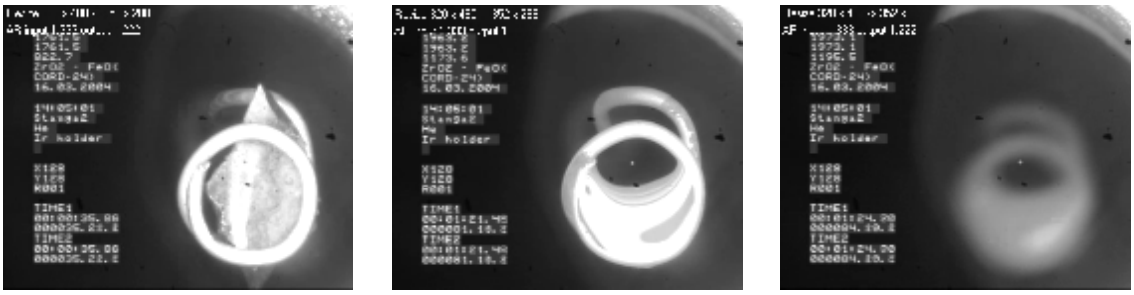

1761.5°C 1963.2°C 1973.1°C (quenching)

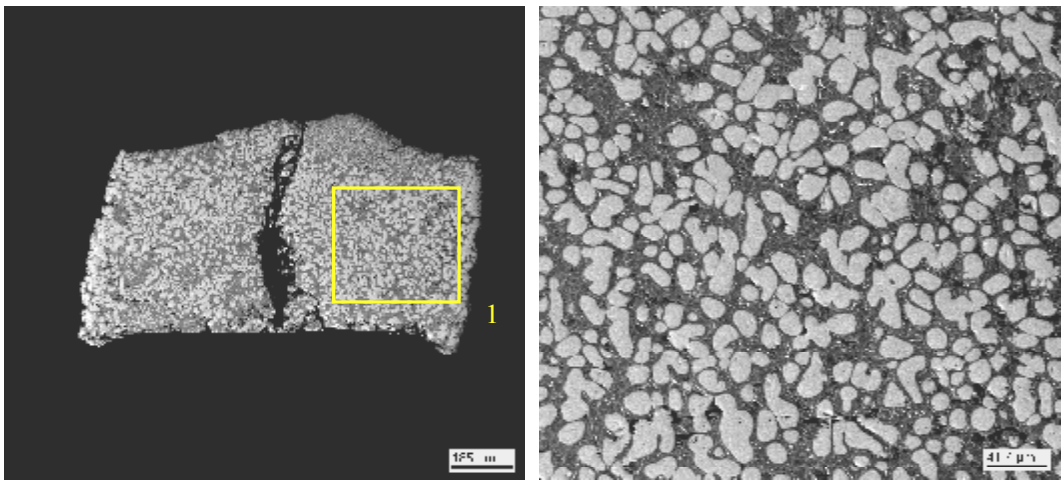

1(SQ1)

Fig. 3.7. Melting in the microfurnace and micrographs of scale from rod sample No. 2 after quenching

Table 3.3. EDX results for scale from rod sample No. 2 after quenching

No.		ZrO_2	FeO	WO_3
SQ1	mass %	57.18	41.14	1.68
	mol.%	44.26	55.05	0.69

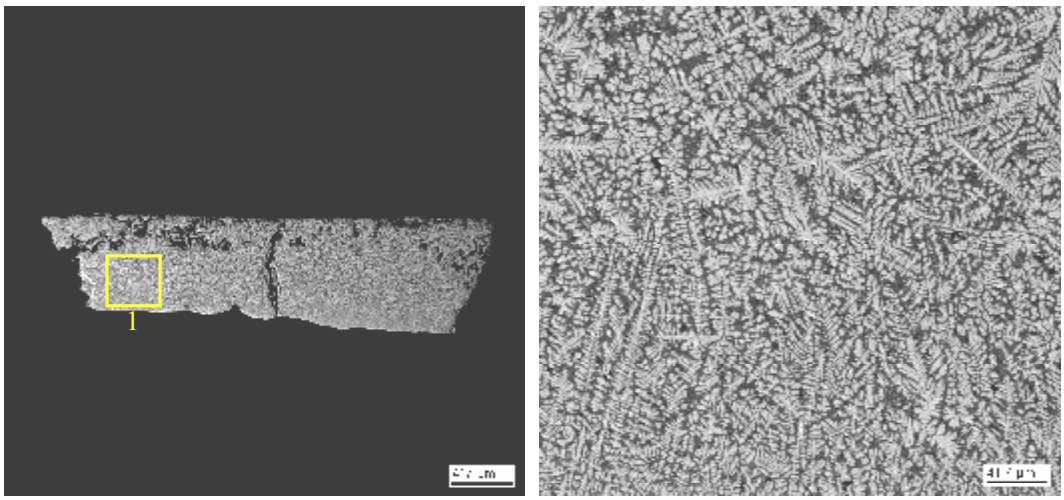

1(SQ1)

Fig. 3.8. Micrograph of scale from sample No. 3 before the microfurnace test

Table 3.4. EDX results for scale from sample No.1 before the microfurnace test

No.		ZrO_2	FeO
SQ1	mass %	53.71	46.29
	mol.%	40.16	59.84

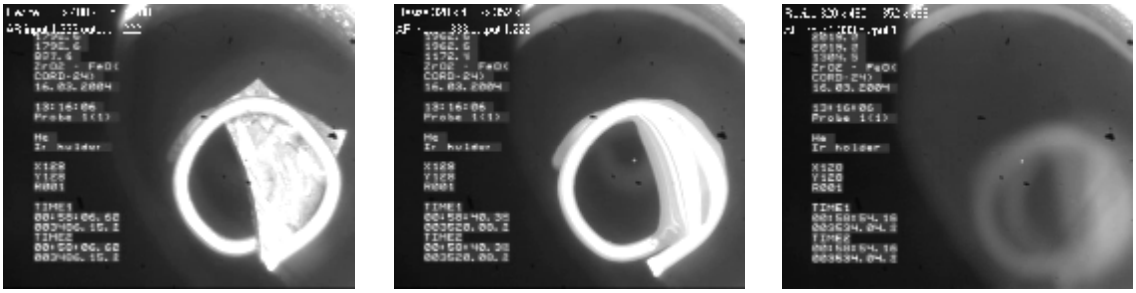

1798.6°C 1962.6°C 2019.0°C (quenching)

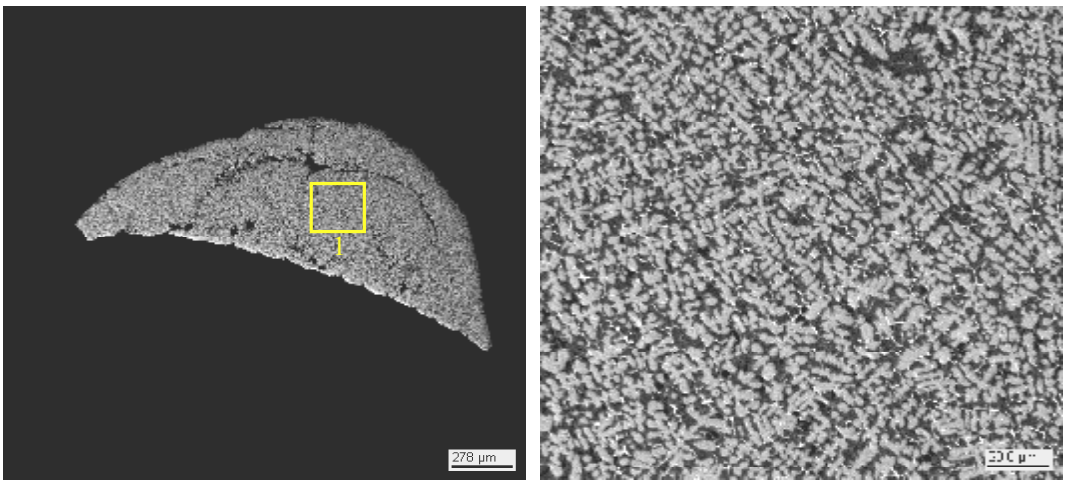

1(SQ1)

Fig. 3.9. Melting in the microfurnace and micrographs of scale from sample No.3, quenching from 2019°C

Table 3.5. EDX results for scale from sample No.3, quenching from 2019°C

No.		ZrO_2	FeO	WO_3
SQ1	mass %	48.64	47.72	3.64
	mol.%	36.55	62.00	1.45

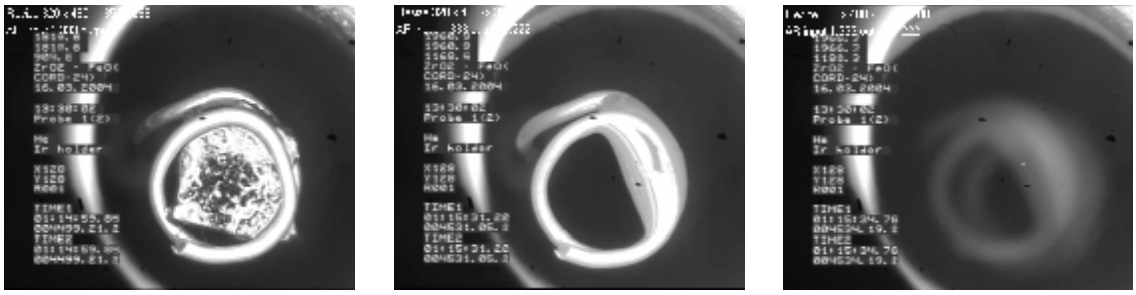

1798.6°C 1960.9°C 1966.7°C (quenching)

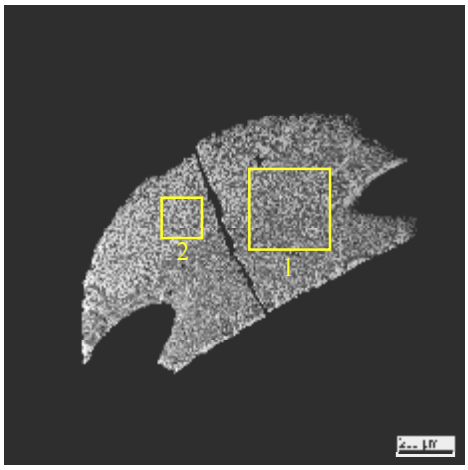

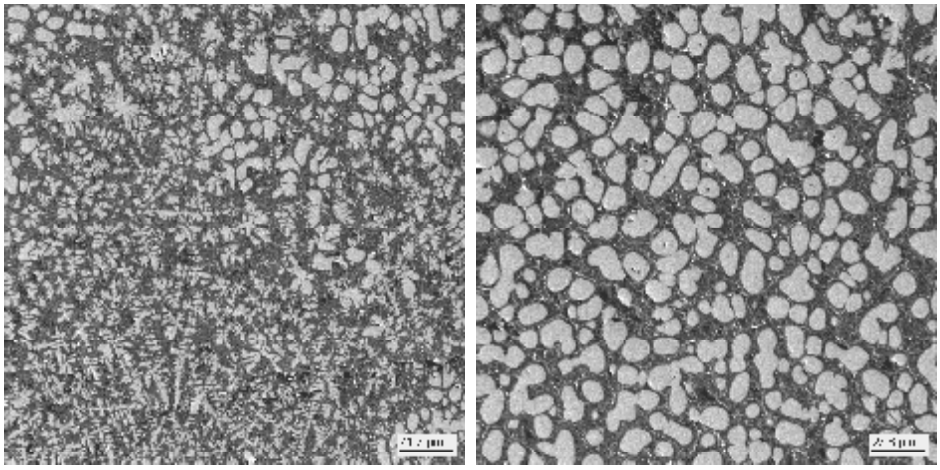

1 (SQ1) 2 (SQ2)

Fig. 3.10. Melting in the microfurnace and micrographs of scale from sample No.3, quenching from 1967°C

Table 3.6. EDX results for scale from sample No.3, quenching from 1967°C

No.		ZrO_2	FeO	WO_3
SQ1	mass %	44.35	54.35	1.30
	mol.%	31.91	67.59	0.50
SQ2	mass %	55.01	43.69	1.30
	mol.%	41.92	57.56	0.52

CORD29A

In order to specify the cub. SS →tetr. SS transition temperature, samples of the high-temperature FeO cubic SS in ZrO_2 synthesized in CORD 29A were subjected to thermal treatment in the Galakhov microfurnace using a special technique. For this purpose, scales were prepared from the crucible regions 2 (Fig.2.34) and 4 (Fig 2.36). Observation of the samples' surface when annealing them at 1850 °C, 1800 °C and 1750 °C for 30 min in the Galakhov microfurnace revealed no changes in the shape of samples' sharp edges. Quenching from said temperatures was followed by the SEM/EDX analysis which also showed no liquid phase isolation along grain boundaries. (Fig.3.11-3.14). The temperature of cub. SS →tetr. SS transition could not be specified by the used method.

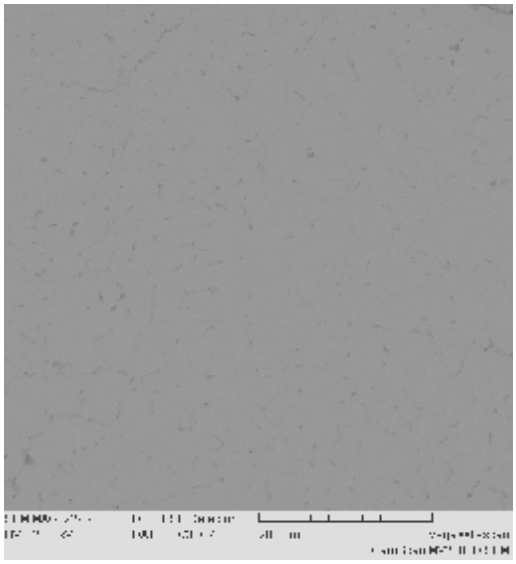

1(SQ1)

No.		Zr	Fe	O
SQ1	mass %	60.56	1.17	38.27
	mol.%	21.58	0.68	77.74

Fig. 3.11 Micrograph of scale (initial). EDX results

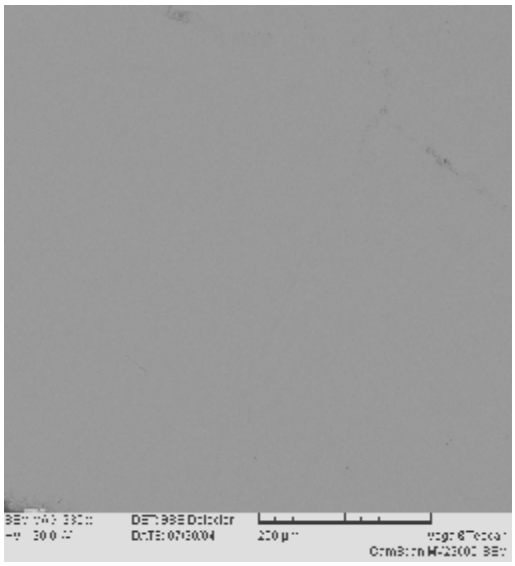

2(SQ1)

No.		Zr	Fe	O
SQ1	mass %	62.3	0.47	37.23
	mol.%	22.63	0.28	77.1

Fig. 3.12 Micrograph of scale (quenching after 10-min exposure at 1750 °C). EDX results

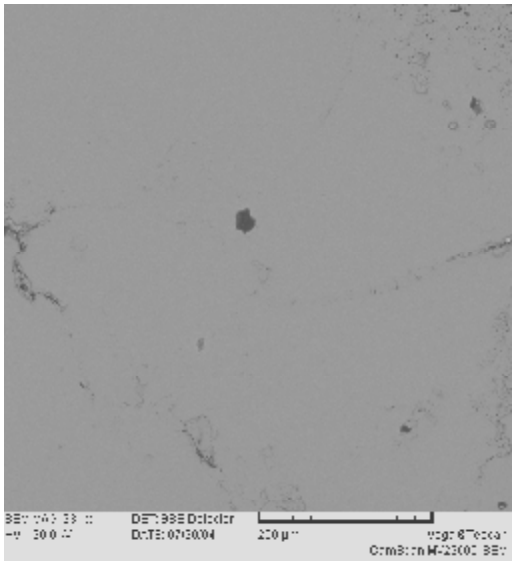

3(SQ1)

No.		Zr	Fe	O
SQ1	mass %	62.66	0.51	36.83
	mol.%	22.91	0.31	76.78

Fig. 3.13 Micrograph of scale (quenching after 10-min exposure at 1800 °C). EDX results

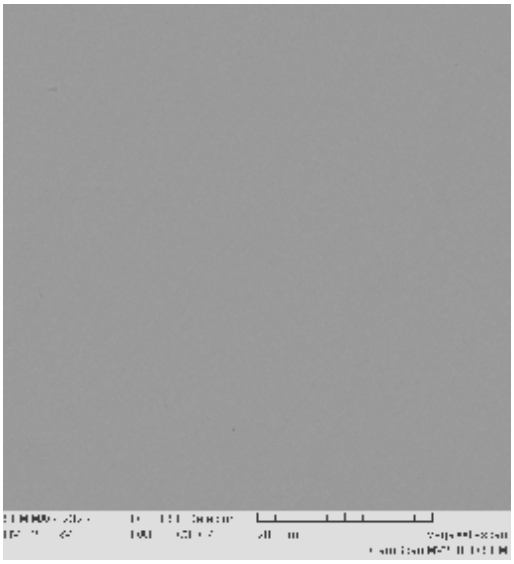

4(SQ1)

No.		Zr	Fe	O
SQ1	mass %	62.38	0.44	37.18
	mol.%	22.68	0.26	77.06

Fig. 3.14 Micrograph of scale (quenching after 10-min exposure at 1850 °C). EDX results

4. Differential thermal analysis (DTA)

For measuring T_{sol}/T_{liq} in the ZrO_2-FeO system, samples from CORD 2, CORD 4 and CORD 9 were subjected to the DTA analysis using the instruments HTA and DSC, Netzsch, Simultaneous Thermal Analyzer STA 429.

Specifications of the equipment used for analyzing samples from CORD 2 and CORD 4:

HTA analyzer. Sample mass ≈ 10-15 mg, pressurized measuring cell, heating rate – 40 °C/min, thermocouple type – W/Re - 5/20. The instrument was pre-calibrated against the standard substances melting points.

Specifications of the equipment used for analyzing samples from CORD 9:

DSC analyzer, Netzsch. Sample mass ≈ 30 mg, purging of the measuring cell with an inert gas, heating rate – 5 °C/min, thermocouple type – B (Pt/30%Rh - Pt/6%Rh). The instrument was pre-calibrated against the standard substances melting points.

The circumstances that considerably complicated the DTA application in studies of the ZrO_2-FeO system at temperatures above 1700 °C are as follows:

- the forming melt was wetting well all the used crucible materials and it lead to the run-out of the liquid phase from crucibles and damage to the instruments;

- the attempts to select a crucible material that would not interact with the melt and contaminate the sample failed.

Therefore, only T_{sol} could be reliably measured by this method.

Thermogram examples are given in Figs. 4.1-4.3.

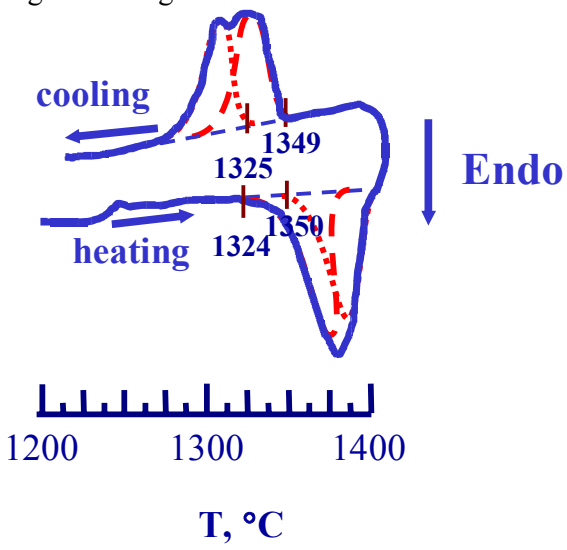

Fig. 4.1. DTA curves of CORD 2 samples from region 1-1, Fig. 2.20. Heating and cooling at 40 C/min

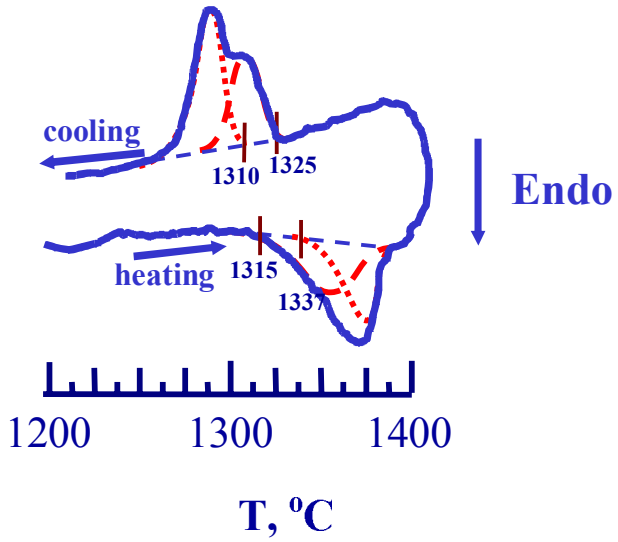

Fig. 4.2. DTA curves from CORD 2, eutectic region 2-1-1, Fig. 2.21. Heating and cooling at 40 C/min

A specimen for the DSC analysis was prepared from a sample taken from eutectic zone 1 of the ingot. Fig. 4.3. shows a thermogram fragment. The measured T_{sol} was 1330 °C

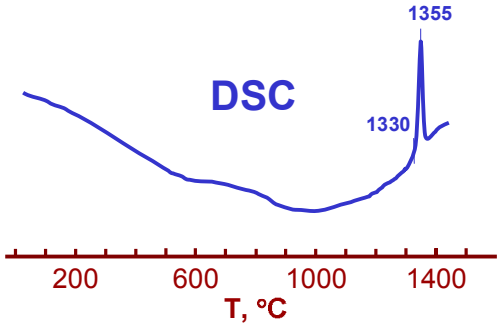

Fig. 4.3. DSC curve of CORD 9 sample from eutectic zone (inert atmosphere)

Note the second peaks in the thermograms (Figs. 4.1-4.2) which prove that the samples' content does not correspond to the eutectic. These and the solidus peaks overlapping causes an additional error in T_{sol} determination by DTA (found to be between 1315-1324 °C). This is why the DTA of samples from the CORD 2 ingot with a small eutectic nucleus was supplemented with the DSC analysis using a more sensitive Netzsch analyzer (Fig. 4.3.). It is seen from the figure that the sample's content is identical to the eutectic and the eutectic temperature equals 1330 °±5C.

5. Discussion of results

The SEM/EDX results for the samples quenched after the measurements in the Galakhov microfurnace indicate a possibly incomplete melting of the samples and their contamination with tungsten oxide, thus making doubtful the T_{liq} values obtained by this method. High chemical activity and fluidity of molten ZrO_2-FeO within the T_{liq}/T_{sol} range are obviously responsible for the significant methodical error of the measurements.

In this relation, it was decided to perform additional studies using the modernized Galakhov microfurnace with differently designed heaters and automated heating control. In order to prevent oxidation of the W heater and the transfer of tungsten oxide to the sample under heating, the protective Ar+4 w%H_2 atmosphere was used (instead of pure argon with partial oxygen pressure of 10^{-4} bar). The data from the additionally performed Galakhov tests are illustrated in Figs. 5.1 – 5.5

CORD5. (Sample from the quenched melt central zone. Fig. 2.13)

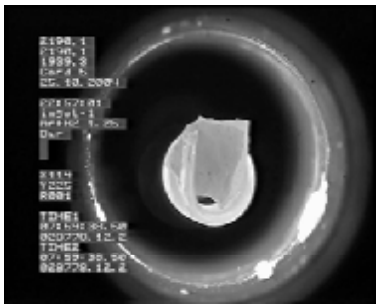

2190.1°C

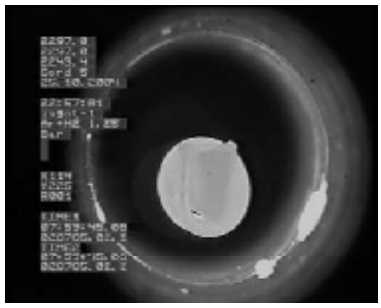

2297°C

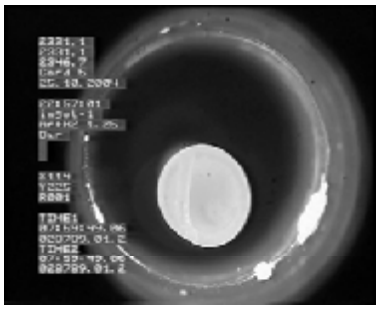

2331.1°C

No.		ZrO_2	FeO
SQ	mass %	70.9	29.1
	mol. %	58.7	41.3

Fig. 5.1. View of sample in holder during VPA in the Galakhov microfurnace. EDX results for the quenched sample

CORD10 (Specimen prepared from the melt sample)

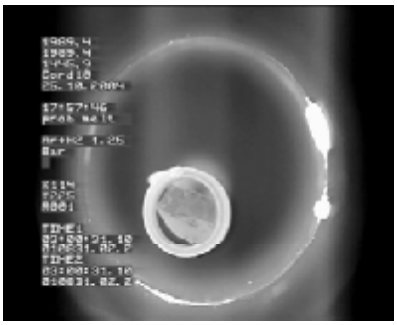

1989.4°C

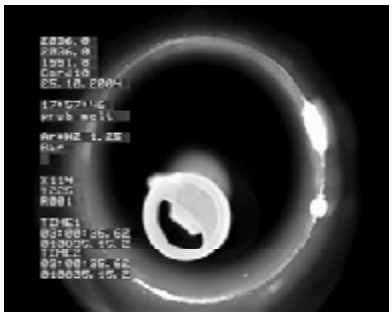

2036.0°C

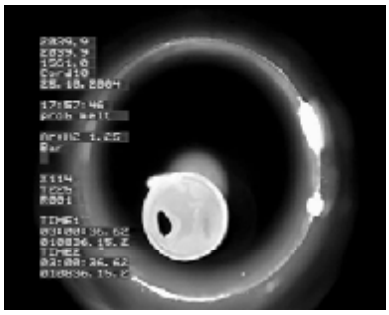

2039.9°C

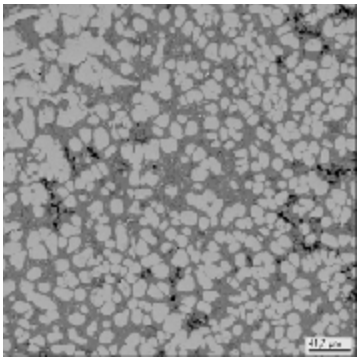

SQ

No.		ZrO_2	FeO
SQ	mass %	44.2	55.8
	mol. %	31.6	68.4

Fig. 5.2. View of sample in holder during VPA in the Galakhov microfurnace. SEM/EDX results for the quenched sample

CORD12 (Specimen prepared from the melt sample).

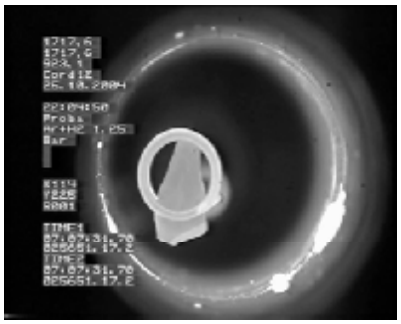

1717.6°C

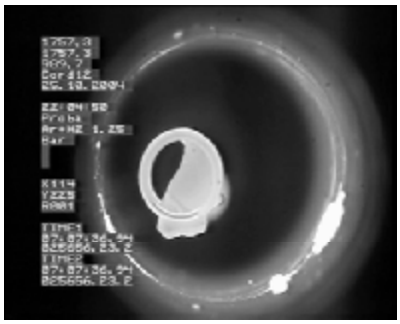

1757.3°C

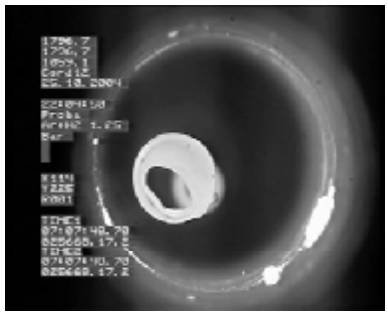

1796.7°C

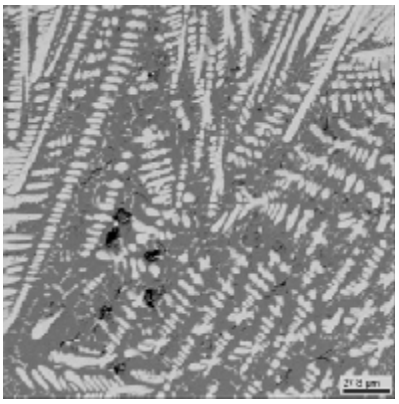

SQ

No.		ZrO_2	FeO
SQ	mass %	29.6	70.4
	mol. %	19.7	80.3

Fig. 5.3. View of sample in holder during VPA in the Galakhov microfurnace. SEM/EDX results for the quenched sample

CORD13 (Specimen prepared from the melt sample).

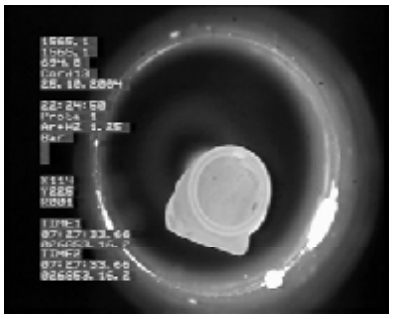

1565.1°C

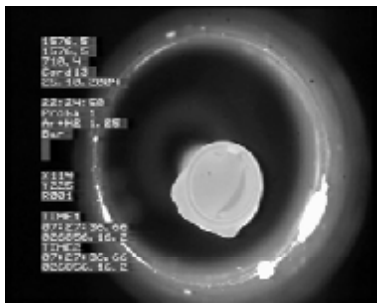

1576.5°C

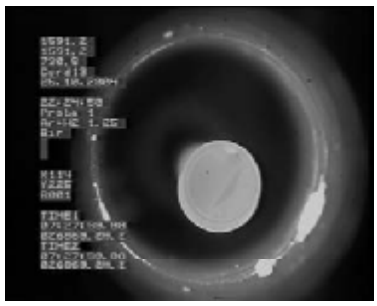

1591.2°C

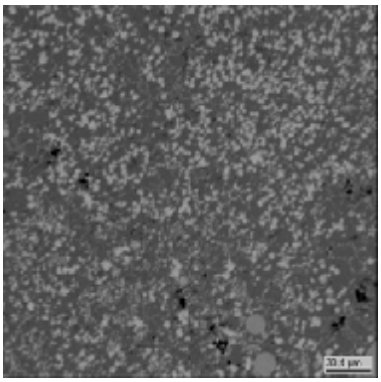

SQ

No.		ZrO_2	FeO
SQ	mass %	21.4	78.6
	mol. %	13.7	86.3

Fig. 5.4. View of sample in holder during VPA in the Galakhov microfurnace. SEM/EDX results for the quenched sample

CORD24 (Specimen prepared from the melt sample).

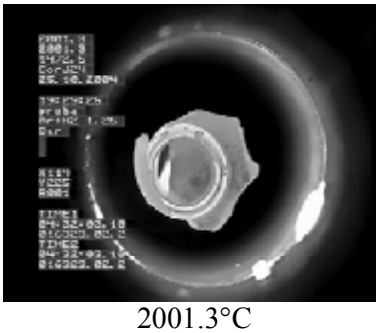

2001.3°C

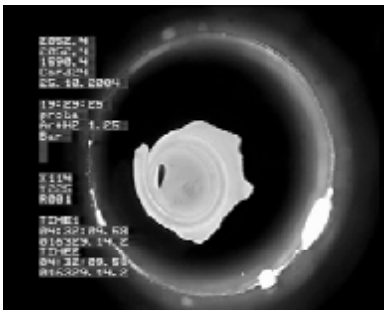

2052.4°C

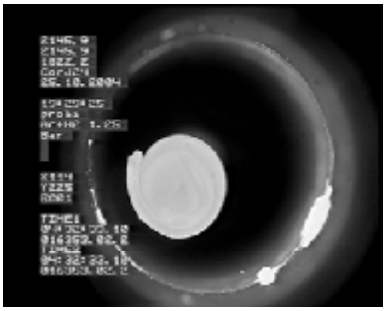

2145.9°C

No.		ZrO_2	FeO
SQ	mass %	62.9	37.1
	mol. %	49.7	50.3

Fig. 5.5. View of sample in holder during VPA in the Galakhov microfurnace. EDX results for the quenched sample

The analysis of T_{liq} values measured in the modernized Galakhov microfurnace shows them to agree well with those obtained by VPA IMCC.

Therefore, the constructed liquidus line of the system in question was based on the results of VPA IMCC, VPA in the Galakhov microfurnace and DTA. The results of measurements by different methods are presented in Tab. 5.1.

Table 5.1. Results of measurements by different methods

Test	Method	FeO concentration		Concentration error, mass %	T_{liq}	T_{sol}
		mass %	mol. %			
CORD 2	**DTA**	-			-	1315
CORD 9	**DSC**					1330
CORD 13	**VPA IMCC**	77.4	85.5	± 3.9	1605	-
	VPA Galakhov	78.6*	86.3	± 3.9	1591	
CORD 12	**VPA IMCC**	68.2	78.6	± 3.4	1793	
	VPA Galakhov	70.4*	80.3	± 3.5	1797	
CORD 4	**VPA IMCC**	54.0*	66.8	± 2.7	2030	
CORD 10		53.5	66.4	± 2.7	2020	
CORD 10	**VPA Galakhov**	55.8*	68.4	± 2.8	2040	
CORD 24		37.1*	50.3	± 1.9	2145	
CORD 24	**VPA IMCC**	44.6	58.0	± 2.2	2112	
CORD 15		41.8	55.2	± 2.1	2161	
CORD 5		31.3*	43.9	± 1.6	2300	
CORD 5	**VPA Galakhov**	29.1*	41.3	± 1.5	2331	
CORD 16	**VPA IMCC**	19.1	28.8	± 1.0	2463	

*). According to SEM/EDX results

The error upper bound of T_{liq} determination by VPA IMCC is +50°C, while the lower one is 1% of the determined value. The error of T_{sol} (eutectic temperature) determination by DTA is ±5°. The error of T_{liq} measurement by the Galakhov method is ±25°C.

After the SEM/EDX analysis of the CORD 2 ingot, charge composition was determined for CORD 9 which was aimed at specifying position of the eutectic. According to the results of this test, the eutectic zone composition corresponds to the FeO content of 83.3±0.5 mass %. Noteworthy is that there is practically no difference between the value of eutectic temperature determined in the present research and that indicated in work [1], while there is a notable difference between the eutectic compositions.

Three forms of ZrO_2, i.e. monoclinic, tetragonal and cubic, are known to exist in the system at different temperatures. The temperatures of polymorphous monoclinic→tetragonal and tetragonal→cubic transformations are equal to 1172 °C and 2347 °C, respectively [18].

Polymorphism of zirconium oxide complicates studying the solubility limit of iron oxides in it. The subsolidus domain of SS existence was not studied in the present work, only the ultimate solubility of iron oxides in the course of crystallization from the melt has been determined. The SEM/EDX and XRF results concerning FeO content in the ZrO_2-based SS are given in Tab. 5.2.

Table 5.2. FeO concentrations in the ZrO_2-based SS (SEM/EDX and XRF results) and lattice parameters (XRD results)

Sample	Characteristic temperature of crystallization start, ℃	Maximum FeO content in ZrO_2, mass %	Maximum FeO content in ZrO_2, mol. %	Structure	Unit-cell parameters
CORD 2, ingot sample after slow crystallization	~1315	1.3	2.2	Not measured	
CORD 4, quenched melt	~2030	6.6-7.2	10.8-11.7	Cub	a = 5.085±0.006 Å V = 131.4±0.5 Å^3
CORD 4 *	~2030	6.4	10.5		a=5.09±0.04 Å V=132±3 Å^3
CORD 5, quenched melt	~2300	5.5-5.7	9.1-9.4		a = 5.08±0.01 Å V = 131±1 Å^3
CORD 9 ingot sample after slow crystallization	~1330	1.3	2.2	tetragonal → monoclinic	a=5.20 Å; b=5.09 Å; c = 5.326 Å; β=99.0° V = 139.13 Å^3
CORD 24 ingot sample after slow crystallization	2030	8.0	13.0	Not measured	
CORD12 ingot sample	1793	10.7	17.0	Not measured	

* - according to XRF results (see Item 2.4.4)

▭ - tests with slow melt crystallization

The solubility limit of iron oxide (II) in zirconia (8.0 mass % FeO) found in the CORD 24 ingot corresponds to a melt in equilibrium with the solid phase, composed (mass %) of 44.2 ZrO_2 + 55.82 FeO (see Tab. 2.9 SQ3).

No ZrO_2 SS in FeO has been found, i.e., the system in question is characterized by the presence of only the ZrO_2-based SS. The maximum values of solubility limit of FeO in ZrO_2 are:

- 1.3 mass % FeO in tetragonal form at eutectic temperature;
- from 8.0 to 10.7 mass % FeO in cubic form.

The cubic solution has been recorded in many tests, but still refined data on its equilibrium composition and the lower boundary of its existence range are required. In CORD 12, when the melt crystallized in the crucible under nonequilibrium conditions after the HF heating disconnection, the maximum solubility of FeO in ZrO_2 was determined (Tab. 5.2), and the

SEM/EDX results showed FeO isolation inside the SS grains. These findings, as well as the results of T_{liq} measurements in CORD 12 allow the supposition that the cubic→tetragonal SS transformation temperature is either lower or equal to 1800 °C. The low-temperature monoclinic ZrO_2 does not form a SS with FeO, and this finding corroborates the results of work [1].

Conclusions

1) On the basis of the experimental data, a quasibinary phase diagram for the ZrO_2 – FeO system has been constructed. It is defined as a diagram with eutectic and bounded areas of FeO SS in 2 forms of ZrO_2

2) The eutectic composition and temperature in the system have been determined. They correspond to 83.3±0.5 mass % of iron oxides concentration and 1330±5 °C

3) The parameters of FeO SS in ZrO_2 have been determined as follows:
   - The cubic SS exists in the temperature interval from 2710 to 1800 °C, the maximum value of FeO solubility limit in ZrO_2 is in the FeO concentration range from 8.0 to 10.7 mass % at ~1800°C;
   - The tetragonal SS exists in the temperature interval from 2347 to 1172 °C, the maximum value of FeO solubility limit in ZrO_2 is 1.3 mass % at 1330 °C (eutectic temperature).

4) No ZrO_2 SS in FeO has been found

5) The obtained results may be used for optimization of phase diagram databases

Fig. 5.6 presents the fusibility diagram for the ZrO_2 - FeO system constructed on the basis of experimental data obtained by different methods.

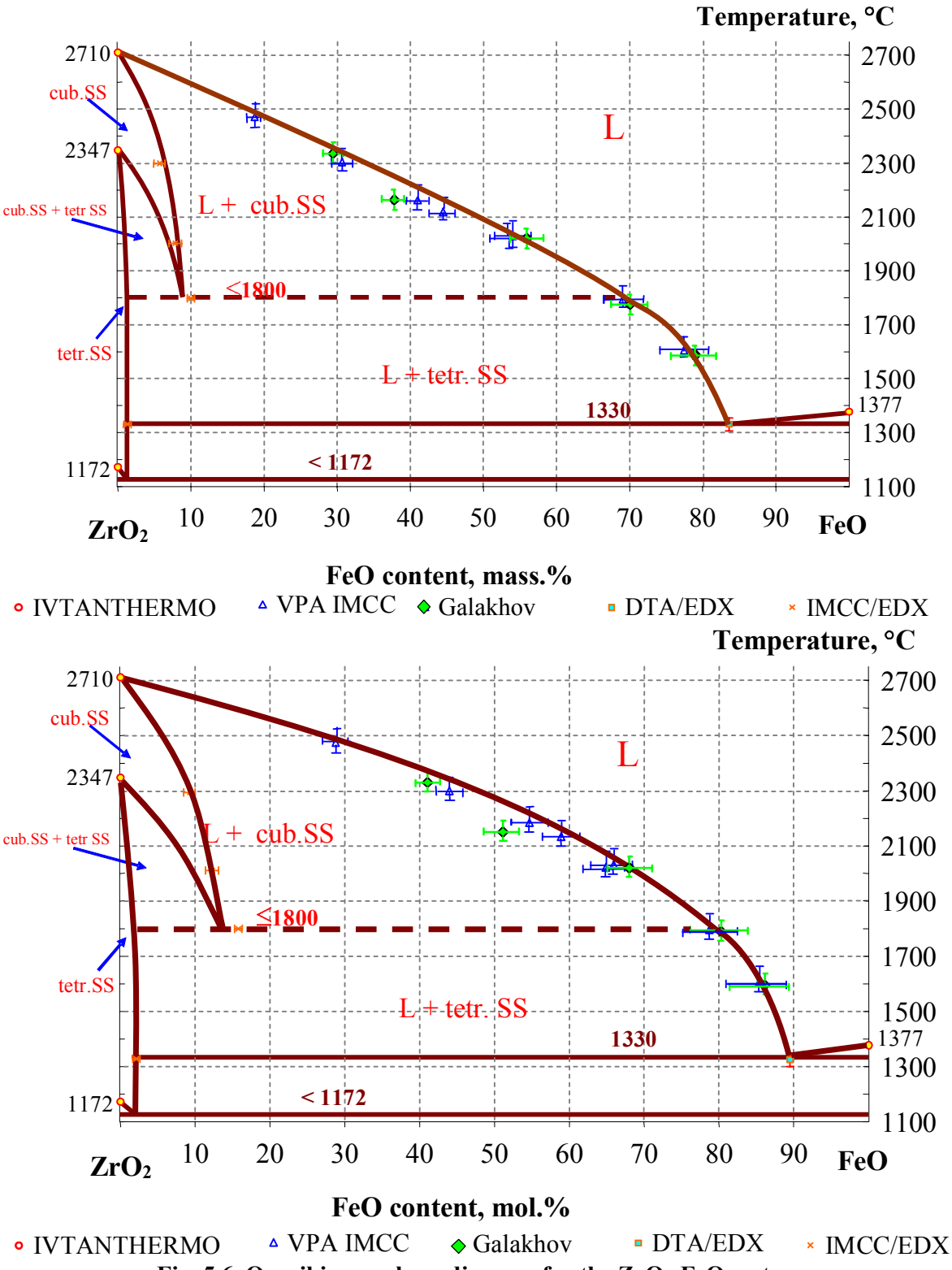

Fig. 5.6. Quasibinary phase diagram for the ZrO_2-FeO system

References

1. W.A.Fischer, A.Hoffman, Archiv Eisenh□ttenw., 28 No739, 1957.
2. New Experiments on the Interaction of ZrO_2 Material with Corium Melts and Phase Diagram Points in UO_2-Based Systems. CIT Project Report, Corium Interactions and Thermochemistry, In-Vessel Cluster, INV - CIT(99)-P037, December 1999.
3. N.M. Voronov et al. High-temperature chemistry of uranium oxides and their compounds, M.:, Atomizdat Publishers, 1971. (Rus.)
4. L. M. Viting. High-temperature solutions and melts.// M.: Moscow State University Publishers, 1991. (Rus.)
5. Generation of data for phase diagrams of multi-component oxidic mixtures, based on prototypic molten corium. ENTHALPY Project report: "European Nuclear Thermodynamic Database validated and applicable in Severe Accidents" First stage, LSK, May 2001.
6. Generation of data for phase diagrams of multi-component oxidic mixtures, based on prototypic molten corium. ENTHALPY Project report: "European Nuclear Thermodynamic Database validated and applicable in Severe Accidents" Second stage, LSK, March 2002.
7. Generation of data for phase diagrams of multi-component oxidic mixtures, based on prototypic molten corium. ENTHALPY Project report: "European Nuclear Thermodynamic Database validated and applicable in Severe Accidents" Third stage, LSK, December 2002.
8. Liquidus and solidus temperature measurements in the subsystem UO_2-ZrO_2-(SiO_2-FeO_x-CaO-Al_2O_3-Cr_2O_3). ENTHALPY Project Report, European Nuclear Thermodynamic Database, Tasks 2.2.3, 2.4 and 2.5.1, SAM–ENTHA(03)–D011, June 2003.
9. Stepanova S. V., Tsivinsky Yu., Zatulovsky L. M., Kopylov V. A., Kravetsky D. Ya. Determination of the temperature axial gradient and the degree of supercooling at the crystallization front in sapphire crystals production by the Stepanov method // Kristallografiya J. (Crystallography), 1982, V.27, Issue 3. pp. 578-583. (Rus.)
10. M.V.Pikunov. Metals melting, alloys crystallization, ingots solidification. M. MISIS. 1997. (Rus.)
11. New miscibility gap for ex-vessel corium oxide compositions"-Y. Petrov, Y. Udalov, K. Jurek, P. Sazavsky, M. Kiselova, P. Selucky , C. Journeau, P. Piluso\\ ICAPP' 04 , Pittsburgh, PA USA, June 13-17, 2004. Paper 4077
12. Galakhov F. Ya. A high-temperature microfurnace for studies of heterogeneous equilibriums in refractory oxidic systems. In: Modern methods of silicates and construction materials analysis // M.: 1961 pp. 178-182. (Rus.)
13. Fyodorov A. A. New methods of metallic powders and slags analysis // M.: Metallurgiya Publishers, 1972. (Rus.)
14. Markov V. K. et al. Uranium. Methods of its determination // M.:, Atomizdat Publishers, 1964. (Rus.)
15. Sendel E. Methods of metal traces determination by colorimetry // M.: Mir Publishers, 1964 (Rus.)
16. Harvey, Smart, Amis, Anal. Chem., 27, 26 (1955).

17. Pozhydayeva O. V., Korytkova E. N., Drozdova I. A., Gusarov V. V. The influence of hydrothermal synthesis conditions on the phase state and particle size of superdispersed zirconia // J. of Gen. Chem. (Zhurnal obshchei khimii). 1999. V.69. Issue 8. pp.1265-1269. (Rus.)

18. Gurvich, L.V., Iorish, V.S. et al. IVTANTHERMO - A Thermodynamic Database and Software System for the Personal Computer. User's Guide. CRC Press, Inc., Boca Raton, 1993.